ENSO Influence over the Pacific North American Sector:

Uncertainty due to Atmospheric Internal Variability

Hosmay Lopez[1,2] and Ben P. Kirtman[2]

[1]National Oceanic and Atmospheric Administration-Atlantic Oceanographic and Meteorological Laboratory, 4301 Rickenbacker Causeway, Miami, FL 33149

[2]University of Miami-Cooperative Institute for Marine and Atmospheric Studies, 4600 Rickenbacker Causeway, Miami, FL 33149

For publication in

Climate Dynamics

Abstract

The relative influence of El Niño Southern Oscillation (ENSO) forced response versus internally generated atmospheric variability or noise on the upper tropospheric Pacific North American circulation is investigated. The analysis is performed on the boreal winter (December-January-February) 200 hPa circulation and the associated precipitation based on observational records and modeling experiments. The model experiment includes an ocean eddy-resolving coupled general circulation model (CGCM) and an atmospheric noise reduced ocean eddy-resolving CGCM. The noise reduction technique is the interactive ensemble approach, adopted to reduce the effects of internal atmospheric dynamics noise at the air-sea interface. Tropical rainfall anomalies associated with ENSO forces a teleconnection pattern that is a combination of the so-called Pacific North American (PNA) pattern, themed here as state-dependent atmospheric noise, and a pattern distinct from the PNA, themed here as ENSO-signal. The ENSO signal has a meridional structure in the streamfunction associated with significant poleward Rossby wave flux emanating from the eastern Pacific. Conversely, the PNA teleconnection pattern is zonally oriented, with most of the wave flux in the zonal direction from the Pacific towards North America. The mid-latitude ENSO forced response is asymmetric between warm and cold events. This asymmetry is strongly dependent on the amplitude of atmospheric noise. It is shown that the ENSO forced response is masked by atmospheric noise, with the latter being 3 to 10 times larger in amplitude. We show that the PNA pattern was positive during the 2015-16 boreal winter and prevented the large 2015-16 El Niño event from alleviating the persistent drought in the western US.

1. Introduction

The southwestern US has recently experienced one of its worst drought periods (2012-present) on record (Griffin and Anchukaitis, 2014; Diaz and Wahl, 2015; Seager et al., 2015). This region is especially susceptible to drought induced soil moisture deficits, enhancing the likelihood for wildfires (Westerling et al., 2006), as observed by the recent widespread forest fires that caused significant loss of human life and negative economic and ecologic impacts. Consequently, the climate community is making an effort to understand the causes for this multi-year drought (Robeson, 2015; Lee et al., 2018).

Several studies have argued that the El Niño Southern Oscillation (ENSO)-related sea surface temperature anomaly (SSTA) and the Pacific Decadal Oscillation (PDO) are the main source of seasonal predictability of winter precipitation over the western US precipitation (McCabe and Dettinger, 1999; Kam et al., 2014). Recent studies have focused on other atmospheric and oceanic patterns that could influence western US droughts. For example, Wang and Schubert, 2014 suggested that north Pacific SSTA influences California droughts. Piao et al. (2016) found significant negative correlation between droughts and the Pacific North American pattern (PNA) and East Pacific wave-train on interannual and decadal timescales after removing the effect of ENSO and the PDO. Lin et al. (2017) found that the synchronization of the signs of the PNA and the North Pacific Oscillation collectively modulate but do not directly cause variations in the upper-atmosphere high-pressure (ridge) that accompanies western US droughts.

As summarized above, a consensus has not been reached regarding which climate pattern (e.g., ENSO or internal atmospheric variability like the PNA) modulates rainfall over the western US. To add further complications, there is still a debate regarding the role of ENSO in forcing the seasonal mean atmospheric circulation over the Pacific-North American sector. One school

of thought argues that ENSO forcing simply serves to amplify internal variability and cannot generate new patterns (Molteni et al., 1993; Lau, 1997; Blade, 1999; Palmer, 1999). In contrast, Straus and Shukla (2002) argue that the atmospheric response to external forcing (e.g., ENSO-related) can lead to patterns distinct from those associated with internal variability (e.g., the PNA). Separating the internal and externally forced pattern was difficult given the lack of sensitivity of earlier General Circulation Models (GCMs) to tropical SSTA forcing. This led to the impression that the ENSO-forced pattern was not distinct from the internally generated PNA pattern, with the forcing simply amplifying the PNA (Lau and Nath, 1994).

The effect of tropical Pacific SST variability on extra-tropical circulation is possible via atmospheric Rossby wave propagation forced by anomalous precipitation and upper–level divergence (Trenberth et al., 1998; Sarachik and Cane, 2010). A consensus has been reached regarding the spatial structure of atmospheric response to tropical heating. During El Niño events, the sub-tropical Pacific jet stream shifts over the western coast of the United States, influencing weather and climate over North America (e.g., Schubert et al., 2004a, 2004b; Seager et al., 2005a, 2005b, 2008; Herweijer et al., 2006).

Variations in tropical Pacific SST occurs on various time scales (Philander, 1990, Trenberth, 1990; Mantua and Hare, 2002). These variations introduce complex atmospheric teleconnection patterns that also have a broad spectrum of time-scales (Barlow et al., 2001; Wu et al., 2003; Chen et al., 2008; Lee et al., 2018). For example, recent literature that focused on low-frequency SST variability showed that the constructive interference of ENSO and the PDO (Mantua et al., 1997) favors enhanced teleconnection patterns over North America. Gershunov and Barnett (1998b) found that El Niño and the positive phase of the PDO favors enhanced

precipitation over the southwestern United States and drought over the Ohio River Valley, with reverse conditions during La Niña and the negative phase of the PDO.

The teleconnection patterns over North America associated with two types of El Niño events is a recent theme in literature. Shift in the location of SSTA can lead to distinct atmospheric responses (Barsugli and Sardeshmukh, 2002, DeWeaver and Nigam, 2004, Lee et al., 2018). Weng et al. (2009) argued that northward shift of the Intertropical Convergence Zone (ITCZ) that brings moisture to the western Pacific is more likely when the El Niño SSTA are located over the central Pacific instead of the canonical eastern Pacific SSTA. Zhang et al. (2012) found that warm SSTA over the cold tongue region has an opposite impact on midlatitude atmospheric circulation than SSTA over the warm pool region with enhanced rainfall over the southwestern United States during the former. Yu and Zou (2013) suggested that there is a more pronounced southward shift of the subtropical jet stream during central Pacific El Niño events. Using a multi-model ensemble forecast system, Infanti and Kirtman (2016) found that model forecasts of 2-meter temperature and precipitation over North America agree more with observations for eastern Pacific El Niño events as opposed to central Pacific events. This is consistent with Lee et al. 2018 which showed that sufficiently warm and persistent SSTA in the far eastern equatorial Pacific is required to excite teleconnection patterns that influence California rainfall.

The preferred internal variability patterns of the mid-latitude atmosphere are considered of high interest for the climate community as they potentially influence weather conditions over a given region on seasonal to interannual timescales. An example of mid-latitude internal atmospheric variability on planetary scale is the PNA teleconnection pattern of Wallace and Gutzler (1981). The PNA includes four main centers of action (as observed by anomalous

200 hPa geopotential height) with strong negative correlation between adjacent centers. This pattern is a dominant mode of variability in GCM, even for simulations with a prescribed SST annual cycle and no interannual boundary forcing. This is further evidence that the PNA is internally generated by the atmosphere (Lau, 1981). This large-scale teleconnection pattern exhibits stronger teleconnection during boreal winter (Gershunov and Cayan, 2003), with significant influence on daily extremes in temperature and precipitation over North America (Gershunov and Cayan, 2003).

Separating the internal atmospheric variability from the SST-forced atmospheric variability is difficult as the former could still be modulated by SST (i.e., state-dependent). An example of such complex interaction is the PNA and ENSO. While the PNA is an internal atmospheric mode, its frequency of occurrence could be modulated by the ENSO state. That is, the PNA contains a state-independent (purely internal) and state-dependent (atmospheric noise modulated by SST) component. One method to separate the internal atmospheric variability from the SST-forced response in coupled models is the Interactive Ensemble (IE) technique of Kirtman and Shukla (2002), this technique is further described in the method section. The IE technique has been used to diagnose the ENSO-Monsoon relationship (Wu and Kirtman, 2003), mechanisms for low-frequency SST variability (Yeh and Kirtman, 2004; Wu et al. 2004; Schneider and Fan, 2007), and the impact of weather noise and model resolution (Lopez and Kirtman, 2015). Lopez and Kirtman (2015) found that ENSO statistics, dynamics, phase locking to the annual cycle, and phase asymmetry are all modified by atmospheric noise and that weather noise is more important in sustaining climate variability as resolution increases.

With regard to model resolution, several studies have found that resolving ocean mesoscale features (i.e., eddies) improve model realizations and climate variability. For example,

resolving ocean eddies improve the local air-sea feedback and the relationship between turbulent heat fluxes and SST (Bryan et al., 2010; McClean et al., 2011; Kirtman et al., 2012; Siqueira and Kirtman, 2016; Putrasahan et al., 2017). Bryan et al. (2010) found a more realistic pattern of positive correlation between high-pass filtered surface wind speed and SST when the ocean component model was eddy-resolving. This suggests significantly different air-sea feedbacks in the presence of realistic ocean eddies. Delworth et a.l (2012) compared simulations of coupled climate model with eddy-resolving, eddy-permitting, and eddy-parameterized resolutions. They found systematic improvements in many aspects of the climate with increasing resolution. Moreover, the IE technique is more efficient in reducing the atmospheric noise forcing as resolution increases as found in Lopez and Kirtman (2015). This is because, at low resolution, the dominant spatial structure of the noise is similar to that of the signal (i.e., noise is masked by the signal). Lopez and Kirtman (2015) also found that weather noise is more important in sustaining climate variability as resolution increases.

The goal of this study is as follows:

- Quantify the relative importance of internally generated versus forced response teleconnection patterns over the Pacific-North American sector and their influence on US winter precipitation.

- Understand the role of atmospheric internal variability in diversifying ENSO-like teleconnections.

- Explain the physical mechanism(s) for why the intense 2015-16 El Niño did not alleviate one of the worst droughts in southwest US history. (more specifically, explain why precipitation was not substantially above the climatological mean in the southwest US/northern Mexico).

The remainder of this paper is organized as follows. A description of the observed datasets and model experiments is given in Section 2. Comparison of observed midlatitude response to ENSO and the PNA is presented in Section 3. Section 4 expands on the previous Section by analyzing coupled model results under atmospheric noise reduction. An analysis of the ENSO response asymmetry is presented in Section 5. Discussion of North America precipitation anomalies associated with ENSO before and after suppression of internal atmospheric noise is presented in Section 6. Summary and discussion is found in Section 7.

2. Data Analysis and Model

a) Observational dataset

We make use of SST data from the Extended Reconstructed Sea Surface Temperature version 5 (ERSSTv5) on a 2° horizontal resolution (Huang et al., 2017). Zonal and meridional winds, geopotential height, temperature, and surface pressure are obtained from the National Center for Environmental Prediction-National Center for Atmospheric Research (NCEP-NCAR) reanalysis (Kalnay et al., 1996), with horizontal resolution of 2.5° (~270 km). We use the Global Precipitation Climatology Centre (GPCC, Becher et al., 2013) precipitation dataset on a 1° grid. All datasets are analyzed for the period from January 1950 to December 2016.

b) Coupled model

The CGCM used in this work is the Community Climate System Model version 4 (CCSM4) from the National Center for Atmosphere Research (NCAR). This is an earth system model consisting of atmosphere, land, ocean, and sea ice components all linked by a flux coupler, which exchanges daily information among the components interactively. The atmospheric component of CCSM4 has 26 vertical levels with horizontal resolution of 0.5°

(zonal resolution is 0.625° and meridional is 0.47°). The atmosphere component employs an improved deep convection scheme by inclusion of sub-grid convective momentum transport and a more realistic dilution approximation for the calculation of convective available potential energy (Neale et al., 2008). The dynamical core uses the finite volume formulation. The ocean model component of CCSM4 uses Parallel Ocean Program version 2 (POP2) numerics (Danabasoglu et al., 2011). The ocean component of the model has horizontal resolution of 0.1, which is eddy resolving. In common terms, eddy-resolving models have horizontal resolution of less than 1/6°. This is significantly higher than the resolution of typical climate modeling experiment, where most models are run at eddy-permitting (resolution of 1/6° to 1°) or even eddy-parameterized resolution (resolution coarser than 1°). This updated version of POP includes a simplified version of the near boundary eddy flux parameterization of Ferrari et al. (2008), vertically-varying isopycnal diffusivity coefficients (Danabasoglu and Marshall, 2007), an abyssal tidally driven mixing parameterization, modified anisotropic horizontal viscosity coefficients (Jochum et al., 2008), and a modified K-Profile Parameterization with horizontally varying background vertical diffusivity and viscosity coefficients (Jochum, 2009). An extended simulation of this ocean eddy-resolving coupled model is described in Kirtman et al. (2012), has been used to understand ENSO precursors in Larson and Kirtman (2013).

c) Noise reduction experiment

We introduce a coupled modeling experiment to further diagnose the North American response to ENSO. A control run is used as a basis for comparison and is referred here forward as HRCTL (high resolution control). This model run is 155 years but the first 100 years are discarded as spin-up (Kirtman et al., 2012; Kirtman et al., 2017). A noise-reduced CCSM4 experiment is also introduce in that the IE technique of Kirtman and Shukla (2002) is employed

in order to filter internal atmospheric variability in the surface fluxes (e.g., momentum, heat, and fresh water). This noise-reduced run is referred here as HRIE (high resolution interactive ensemble, see Kirtman et al., 2017) and is comprised of 50-year model simulation. In principle, the IE technique only affects the variability at the air-sea inter-face. For example, if the simulated SSTA variability in HRIE is comparable to HR, then the atmospheric variability should also be comparable. On the other hand, if the SSTA variability in HRIE is significantly reduced, then in principle we expect there to be some reduction in the ENSO forced atmospheric variability.

The IE strategy uses multiple realizations of the atmospheric model (CAM) coupled to a single realization of the ocean model (POP), multiple realizations of the sea-ice model and the land-surface model. The coupling of multiple realizations to single realizations of the ocean component model is accomplished through the CCSM4 coupler. In the specific application shown here, we use 10 atmospheric realizations coupled to a single realization of the ocean model. The purpose of this coupling strategy is to significantly reduce the stochastic or weather noise forcing of the ocean due to internal atmospheric dynamics. Ensemble averaging of fluxes of heat, momentum and fresh water produced by the individual CAM ensemble members before they are passed to the ocean effectively filters the noise in the fluxes due to internal atmospheric dynamics. The sea-ice and land surface models are also coupled to the ensemble mean fluxes. Additional details can be found in Kirtman et al. (2009), Kirtman et al. (2011) and Kirtman et al. (2017). While the HRIE simulation is only about 55 years in length, the atmosphere internal variability for a particular ensemble member is independent from the other members, so in essence we have 10x55 or 550 years of independent realizations of internal atmospheric variability.

d) Analysis technique

We use Niño3.4 (SSTA averaged from 190°E to 240°E and 5°S to 5°N) for tracking ENSO. The PNA index is defined as in Wallace and Gutzler (1981) by linearly combining four normalized 200 hPa geopotential height anomalies. That is, the PNA pattern is comprised of four centers; one is located near Hawaii (20°N and 160°W), another over the North Pacific Ocean (45°N and 165°W), a third over western Canada (55°N and 115°W), and lastly one over the Southeastern United States (30°N and 85°W). We also make use of the stationary Rossby wave flux defined in Plumb (1985) to assess wave energy propagation in mid-latitude atmosphere. The Plumb flux is a generalized version of the widely used Eliassen-Palm (EP) flux (Andrews and McIntyre 1976) in that it can diagnose the three-dimensional propagation of stationary wave activity on a zonally asymmetric flow field.

As in Plumb (1985), the three-dimensional Rossby wave flux in spherical coordinates follows (1), where P is the pressure in hPa, a is the radius of the Earth in meters, $\emptyset$ represents latitude, λ is longitude, ψ is the streamfunction, Ω is the angular velocity of the Earth and N is the Brunt-Vaisalla or buoyancy frequency.

$$\vec{F} = P \begin{pmatrix} \frac{1}{2a^2 cos\emptyset}\left(\left(\frac{\partial\psi}{\partial\lambda}\right)^2 - \psi\frac{\partial^2\psi}{\partial\lambda^2}\right) & \frac{2\Omega^2 sin^2\emptyset}{N^2 a}\left(\frac{\partial\psi}{\partial\lambda}\frac{\partial\psi}{\partial z} - \psi\frac{\partial^2\psi}{\partial\lambda\partial z}\right) \\ \frac{1}{2a^2}\left(\frac{\partial\psi}{\partial\lambda}\frac{\partial\psi}{\partial\emptyset} - \psi\frac{\partial^2\psi}{\partial\lambda\partial\emptyset}\right) & \end{pmatrix} \qquad (1)$$

3. Mid-Latitude ENSO Teleconnection versus Intrinsic Atmospheric Variability

To understand the differences between ENSO forced and internal atmosphere response pattern of boreal winter circulation, we base our analysis on composites. Figure 1 shows the December-January-February (DJF) 200 hPa geopotential height anomaly during (a) positive ENSO events, (b) negative ENSO events, (c) positive PNA winters, and (d) negative PNA

winters. The composite for positive (negative) ENSO events is based on Niño3.4 SSTA larger (smaller) than plus (minus) one standard deviation. Similarly, the PNA composites are defined based on PNA index standard deviation greater than unity. Figure 1 shows that the mid-latitude atmospheric response to ENSO is asymmetric between positive and negative events, as was noted in Straus and Shukla (2002). The response to positive ENSO has larger anomalies over the Northern Pacific, and a more intense Canadian positive height anomaly compared to the negative height anomaly associated with the negative phase of ENSO (Fig. 1b). The asymmetry is also observed in the spatial structure of the height anomalies, with the positive ENSO response having a more meridionally-oriented pattern. For example, the deepening of the Aleutian Low is connected to negative anomalies over the southern US. For the negative ENSO response, the anomalies follow more of a *great-circle* pattern with a clear southeastern US positive pole. The spatial structure of this pattern more closely corresponds to the PNA patterns in Figs. 1c and 1d, with spatial correlation of -0.98 and 0.91, respectively. This suggests that the dominant patterns of the mid-latitude response to tropical heating are related to the preferred internal variability of the atmosphere, at least for the negative phase of ENSO. This asymmetry in ENSO-related atmospheric teleconnection is well documented (Hoerling et al. 1997, 2001; Hannachi et al., 2003; Zhang et al., 2011; Zhang et al., 2014). We also note that the asymmetry (i.e., difference in El Niño and La Niña) of the ENSO teleconnection is comparable in amplitude as that of the symmetric (i.e., combined El Niño and La Niña) component (Zhang et al., 2014). We will return to the issue of asymmetry in ENSO teleconnections later in this article.

There is an important caveat in the analysis presented for Fig.1. The construction of boreal winter atmospheric pattern in Fig. 1 is an unstated assumption that any signature of internal atmospheric variability is assumed to be greatly reduced by compositing multiple cases.

11

Figure 2 shows the time series of Niño3.4 SSTA (color) and PNA (black) from January 1980 to January 2016 and associated power spectra and auto-correlation. The strong El Niño events of 1982/83, 1997/98, and 2015/16 are well depicted in the time series. We also note that some of the warm and cold ENSO events have been accompanied by large amplitude PNA index. However, the strongest PNA on record, which occurred during the winter of 1980/81, was accompanied by relatively neutral ENSO conditions. Spectral density analysis shows that the PNA index closely resembles a white-noise process with nearly equal power at all frequencies. Most of the power for Niño3.4 SSTA occurs on interannual timescales, which is well documented. The lag autocorrelation has a rapid de-correlation (about 1 month) for the PNA index, much shorter than 8-9 months for ENSO.

Separating the effect of ENSO from that internally generated by the atmosphere like the PNA is not trivial. Figure 2a shows that these two processes can co-exist. Also, there is a marginal but significant correlation between the observed Niño3.4 and the PNA index (r=0.33) which suggests that the PNA is not entirely state-independent noise and contains a state-dependent (i.e., ENSO-modulated) component. Here we make use of conditional composites by averaging those winter seasons with extreme ENSO events and little or no PNA pattern. We will refer to these as the ENSO composite hereafter. Similarly, we average those winter seasons with extreme PNA and little or no ENSO events, and referred to as the PNA composite. Our goal for this conditioned composite is to isolate as much as possible the influence of the PNA on ENSO teleconnections and vise-versa. Also, by looking at those winters with little PNA activity, we hoped to have a clearer understanding of the ENSO teleconnection in that it is found to be significantly smaller than those from the PNA and thus more easily masked by the PNA.

12

Figure 3 shows the conditional composite of 200 hPa anomalous streamfunction (contour), horizontal (vector) and vertical (shaded) stationary Rossby wave flux of December-January-February (DJF) seasonal mean during a positive PNA (Fig. 3a) and neutral ENSO, and positive ENSO events and neutral PNA (Fig. 3b). Note that the mid-latitude response to ENSO-related tropical heating (Fig. 3b) as measured by these composites is significantly smaller than that generated internally by the atmosphere (Fig. 3a). The PNA shows a zonally oriented wave-train pattern in the streamfunction. Most of the horizontal wave-flux occurs over the North Pacific towards North America. Vertical wave-flux is upward (downward) over the North America (Gulf of Alaska) region. That is, most of the vertical and horizontal stationary wave flux for PNA winters is located in regions of the major mid-latitude storm track and associated jets with no tropical origin. As suggested in Karoly et al. (1989), jet stream instability or transient eddies interaction with the mean flow are major mechanisms in forcing these anomalous stationary waves.

The ENSO response (Fig. 3b), however, shows a meridionally-oriented structure in the streamfunction, which is in contrast with the zonally oriented structure associated with the PNA pattern. The ENSO response also shows an anomalous anticyclone over most of the subtropics, a feature that is absent for the PNA pattern. The anomalous cyclonic pattern extends from most of the northern Pacific southeastward towards the southeastern United States. There is clear wave flux towards North America with tropical origin, mostly over the eastern Pacific. There is also significant flux from the Northern Pacific, associated with deepening of the Aleutian Low. These two wave fluxes with comparable amplitude converge over the anomalous anticyclone over central Canada.

The analysis presented in Fig. 3 argues that the response to tropical Pacific heating associated with ENSO is significantly different and has smaller amplitude than that internally generated by the atmosphere. Note that we are not suggesting that ENSO and the PNA are independent, given that the PNA index is correlated with the ENSO index (r=0.33), suggesting that ENSO variability also tends to generate a systematic response in the PNA pattern. Although this response is a smaller portion of the total variability of the PNA as the modest correlation suggests. The PNA also occurs as an internal mode of atmospheric variability, hence our motivation in trying to separate the ENSO forced versus the atmospheric internal variability. The IE technique used here is an ideal tool for this task. Since each atmosphere in the IE run is forced by the same SST pattern, any difference among ensemble members is purely intrinsic to the atmosphere (i.e., state-independent). The state-dependent component (i.e., SST dependent) of the PNA is comparably smaller than the state-independent as suggested by the low correlation with ENSO. This is supported by performing an additional model experiment in which climatological SSTs are prescribed to the atmosphere-only model and found that the PNA pattern in the atmosphere-only model run (not shown) is nearly identical in amplitude and spatial distribution as that from observation and ocean-atmosphere coupled simulations. Hence, this highlights the challenge in isolating the component of the PNA that is state-dependent.

Note that the mid-latitude response to ENSO does include both the traditional ENSO forced response (largely independent of the PNA) and a PNA component that has changed because the background state has change (i.e., state-dependent internal variability). Only the later provides a systematic teleconnection pattern, whereas the PNA part is more random and complicates the teleconnection structure, and thus predictions of ENSO remote impacts. Therefore, it is very difficult to establish a well-defined teleconnection pattern because the

ENSO forced response is influenced by the presence of weather noise. In the next section, we make use of the IE noise reduction technique in order to study the ENSO forced response versus internal variability of the atmosphere separately.

4. Noise Reduction

To understand ENSO teleconnections under the IE noise reduction, we first examine the importance of atmospheric noise over the tropical Pacific. Figure 4 describes the symmetric (left-column) and asymmetric (right-column) ENSO components based on the composite of December-January-February (DJF) SSTA for observed (a and b), HRCTL (c and d), and HRIE (e and f). The composite is based on Niño3.4 SSTA larger than one standard deviation. HRCTL symmetric component (Fig. 4c) has maximum SSTA over the central Pacific and similar meridional structure and amplitude as observed (Fig. 4a). SSTA are highly reduced in the HRIE case (Fig. 4e), consistent with Lopez and Kirtman (2015).

We show ENSO phase asymmetry because it is a possible source for the mid-latitude asymmetry seen in Fig. 1. Both HRCTL and HRIE have smaller asymmetry than observed, especially for the interactive ensemble run. For the observed (Fig. 4b), ENSO asymmetry is mostly positive (negative) over the eastern (western) Pacific. The negative pole over the western Pacific is captured in HRCTL and to a minor extent in HRIE. The notion of ENSO asymmetry in CGCMs was thoroughly investigated in Zhang et al. (2009). They found that the lack of asymmetry in CCSM3 (i.e., an earlier version of the CGCM used here) is due to a lack of asymmetry in the zonal wind stress over the central Pacific, caused by a biased representation of atmospheric deep convection associated with SSTA. Lopez et al. (2013) found that the absence of state-dependent westerly wind burst (i.e., a type of atmospheric noise forcing of the tropical Pacific Ocean) in couple models result in a bias towards cold ENSO events.

The reduction of ENSO amplitude and asymmetry due to noise reduction may have repercussions on the extratropical atmospheric response to tropical heating and hence precipitation over the US. That is, the reduced ENSO amplitude leads to reduced tropical heating, which should weaken the Rossby wave forcing hence reducing the remote teleconnection. On the other hand, the noise reduction may facilitate identifying the ENSO-forced pattern in that less noise in the SSTA would translate into a more systematic atmospheric response (e.g., larger signal-to-noise ratio).

We first diagnose the tropical upper atmosphere response to warm SSTA via composite analysis. For this, we look at atmospheric Rossby wave source or forcing function (2), which is comprised of advection of planetary vorticity (i.e., sum of relative vorticity ζ and the Coriolis parameter f) by the divergent wind V_χ (first term in eq. 2) and vortex tube stretching (second term in eq. 2).

$$Rossby\ wave\ source = -V_\chi \cdot \nabla(\zeta + f) - (\zeta + f)\nabla \cdot V_\chi \tag{2}$$

Note from Fig. 5 that the symmetric (i.e., El Niño minus La Niña) component of the wave source is dominated by anticyclonic wave source straddling the equator at about the dateline. Anticyclonic (cyclonic) wave source is negative (positive) in the Northern Hemisphere and the opposite in the Southern Hemisphere. This meridional structure centered at about the equator is caused by meridional planetary vorticity advection due to upper level divergence and driven by warm SSTA. Also note that, both HRCTL and HRIE simulations, accurately depict the spatial pattern of the observed Rossby wave source. Recall that the HRIE simulation produces reduced amplitude ENSO events due to weather noise filtering, hence the smaller amplitude in the wave source.

The asymmetric (i.e., El Niño plus La Niña) component of the wave source is also dominated by anticyclonic wave sources east of the dateline. This is expected as the asymmetric SSTA shown in Fig. 4 looks like the symmetric component east of the dateline. Also, worth noting is that the asymmetry is significantly reduced in the HRIE case (Fig. 5f), as with the SSTA (Fig. 4f), producing a more systematic ENSO teleconnection patter.

For example, Fig. 6 depicts the tropical Pacific composite 200 hPa streamfunction (contour) and relative vorticity (shaded) for the 10 warmest ENSO events. Panels E1 through E10 correspond to each of atmospheric members of HRIE model. The *Emean* panel indicates ensemble mean of the 10 atmospheric ensemble members in the HRIE simulation, whereas CTL panel corresponds to the single atmospheric realization in the HRCTL simulation. Therefore, the ensemble average for the HRCTL is just the average of all El Niño events (10 in this case). So, we should call it composite mean of El Niño events as there is just a single ensemble member in the HRCTL case. In contrast, the HRIE ensemble mean contains the average for 10 El Niño events for each atmospheric ensemble simulation for a total of 100 events. Recall that each atmospheric member is subject to the same boundary forcing from the ocean. Overall, all atmospheres of the HRIE respond similar as HRCTL to tropical heating, with anticyclonic circulation north and south of the equator and associated upper level easterlies about the equator. Differences among ensemble members highlight the fact that each atmosphere member produces its own internal dynamics, although at 200 hPa in the tropics this effect appears to be qualitatively small.

In the same format as Fig. 6, Fig. 7 shows the Pacific North American sector composite of 200 hPa streamfunction (contour) and relative vorticity (shaded) for the same 10 warm ENSO events. By simple inspection, it is easy to observe that all ensemble members have distinct

structure in the streamfunction and vorticity fields. There is arguably only one member (i.e., E2) that has a similar structure as the HRCTL, and most importantly, the ensemble mean of HRIE run is markedly different from HRCTL. Overall, the HRCTL is similar to the observed pattern shown in Fig.1a, whereas the ensemble mean HRIE here is similar to the observed pattern in Fig. 3b. This indicates that the HRCTL pattern is not a clean depiction of midlatitude ENSO response due to the presence of significant internal atmosphere variability as suggested from the large spread among ensemble members. In contrast, HRIE ensemble mean presents a clear ENSO-forced response due to noise reduction from IE and ensemble averaging technique despite a reduction in the amplitude of the tropical SSTA due to atmospheric noise reduction. What remains unclear is whether the spatial structure difference in HRIE ensemble mean is due to some fundamental change in the tropical forcing and response or simply due to a factor of 10 larger ensemble averaging.

Thus far we showed that internal atmospheric dynamics is dominating mid-latitude upper atmosphere, which consequently muddles the true response to ENSO and tropical Pacific heating. The HRIE simulation has the advantage that it is possible to quantify the noise via the individual ensemble members within the context of the coupled system (see Kirtman et al., 2011). Here, we estimate the atmospheric internal variability for each ensemble members following (eq. 3), where *Field* is any variable, *N* is the ensemble size. Note that a noise variable is obtained for each ensemble member *i*.

$$Noise_i = Field_i - \frac{1}{N}\sum_{i=1}^{N} \quad Field_i \, N = 10 \, ensemble \, members \tag{3}$$

Now that we have defined the noise for each atmospheric realization, it is natural to ask what is the basic structure of the noise? To answer this question, we make use of Empirical

Orthogonal Function (EOF) analysis of the noise defined in (eq. 3). Here, the EOF is applied to the DJF (boreal winter) structure of (eq. 3) during 10 El Niño events for the HRIE case. These events are defined as before based on Niño3.4 standard deviation. Since we have 10 ensemble members and 10 El Niño events, we can apply the EOF to those 100 maps (i.e., 10 ensemble members for each El Niño event) since each ensemble member is synoptically independent. Essentially, the atmospheric states are noise independent but signal dependent through the coupling to the same ocean state. Figure 8 depicts the composite of 200 hPa geopotential height anomaly during DJF for warm ENSO events for the HRCTL simulation (Fig. 8a) and the HRIE simulation (Fig. 8b). Figure 8c shows the spatial structure of EOF 1 of internal atmospheric dynamics 200 hPa geopotential height for HRIE simulation. The spatial structure of geopotential height anomaly for HRCTL is very similar to that of observed pattern (Fig. 1a). Here, positive anomalies dominate the tropical upper atmosphere with two negative height anomalies over the Aleutian Low and the southeastern United States. It also shows a positive height anomaly over the Hudson Bay, this is also consistent with observations. For the HRIE case (Fig. 8b), a positive height anomaly is still present over the tropics, but weaker than those from HRCTL due to reduced tropical forcing (Figs. 4 and 5).

The spatial structure of midlatitude atmospheric response is significantly different in the ensemble mean atmospheric composite from the HRIE simulation compared to HRCTL. Among others, there are two possible scenarios for this difference explored here: (1) the differences are rooted in the tropics – something is different in the tropical forcing, or (2) the differences are rooted in the mid-latitudes – the true ENSO-forced response is that of HRIE (Fig. 8b) and HRCTL (Fig. 8a) is contaminated by mid-latitude atmospheric internal dynamics noise. We know that the amplitude of the SSTA in HRIE is smaller but that the deep tropical circulation

response associated with ENSO depicted in Figs. 5 and 6 is similar between HRCTL and HRIE. So, it remains an open question which of the above two possibilities explain the differences in the ENSO response. Ultimately, we argue here that difference is rooted in the tropical forcing. It is, however, instructive to eliminate the possibility that the differences are rooted in the mid-latitudes and are simply just sampling issues. We address this sampling question first below.

While it was shown that ENSO response is systematically different in the HRIE model, we have not yet clarified if this is due to larger sampling in the HRIE (e.g., 10 events times 10 ensemble atmospheres for DJF) compared to HRCTL (e.g., 10 events times 1 atmosphere for DJF). That is, what if we had 90 more ENSO events in HRCTL, would it reproduce the ENSO forced response in HRIE? If that were the case, then simply having more HRCTL events would produce the HRIE pattern. To answer this, a Monte Carlo sampling technique is used in that composites are built by randomly selecting ensemble members from the HRIE case. The composites are built similar to that of HRCTL, but here a random ensemble member is chosen for each of the 10 ENSO events and each of the December-January-February (DJF) months. In total, 30 random maps are composite. There is a total of 300 maps to choose from and those are drawn with replacement. The composite is repeated 5000 times and are named MCE (Monte Carlo ensemble) herein. The goal is to compare whether a randomly chosen ensemble average reproduce the HRCTL pattern (Fig. 8a) or that of the HRIE (Fig. 8b). We will base the comparison in term of spatial correlation of those MCE with that of HRCTL and HRIE patterns.

Figure 9a depicts the probability density function (PDF) for the spatial correlation between MCE and HRCTL composite (red) and the spatial correlation of MCE and HRIE composite (blue) of midlatitude 200 hPa geopotential height anomaly during El Niño events. Note that the PDF of MCE correlated with HRIE is shifted toward unity (e.g., 0.65 mean

20

correlation) compared to that of MCE correlated HRCTL (e.g., 0.31 mean correlation). This argues that the systematic differences between HRCTL and HRIE shown in Figs. 8a and 8b are not due to subsampling of HRCTL, but something more fundamental is occurring in the HRIE run. We will return to this issue at the end of this section.

Another implication from Fig. 7 is the fact that all individual ensemble members from HRIE look quite distinct from each other. In other words, there is substantial atmospheric noise present in the composite. This raises the question whether the noise level in each individual ensemble member is comparable to the HRCTL composite. As noted early, in principle it is possible for HRIE to have smaller signal-to-noise ratio since the tropical forcing could be smaller, but the mid-latitude noise amplitude should be unchanged. To check this, the MCE technique presented earlier is used to calculate signal-to-noise ratio (SNR) of 200 hPa geopotential height. SNR is defined by the ratio of the magnitude of composite 200 hPa geopotential height divided by the standard deviation among events (i.e., event spread) and averaged over the PNA region. Figure 9b shows the PDF of SNR for MCE (black) compared to that of the HRCTL (red arrow). It is obvious that individual ensemble members from HRIE have lower SNR than that of HRCTL in the 200 hPa height over the PNA region. This is due to reduced tropical SST in HRIE while the noise amplitude is similar for both models.

It is important to underscore the results in Figs. 9a and 9b. First, Fig. 9a indicates that the ENSO response in the HRIE spatial structure is indeed different from the HRCTL. Second, and perhaps as expected, the mid-latitude ENSO response SNR in HRIE is considerably smaller than HRCTL. The apparent contradiction comes from the fact that we suggest here (Fig 8 in particular) that the HRIE composite response (Fig. 8b) is a "cleaner" depiction of the ENSO

response and that noise is still contaminating the HRCTL response. Resolving this apparent contradiction is discussed further below.

The leading noise EOF (Fig. 8c) is very similar to the observed PNA pattern (Figs. 1c and 1d) with four poles. We note that the PNA pattern in the CCSM simulations are geographically identical to the PNA pattern identified in observations (not shown). This noise pattern explains 36% of the total noise variance over the Pacific-North America region. The fact that we were able to obtain the PNA pattern from HRIE case via noise EOF and that this pattern is the leading mode suggests that there is still noise variance left in the individual ensemble members after applying the IE noise filtering. This is to be expected because the IE approach does not explicitly attempt to reduce the amplitude of the variability due to internal atmospheric dynamics. Also note that the noise amplitude in Fig. 8c) is still twice as large as the ENSO-forced pattern shown in Fig. 8b), consistent with low SNR in Fig. 9b. This explains the large differences among ensemble members in Fig. 7. It is also worth noting that the pattern in Fig. 8a (i.e., the ENSO composite from HRCTL) appears to be a combination of the patterns from Fig. 8b (i.e., ENSO forced) and Fig. 8c. (i.e., internal atmospheric variability). This suggests that ENSO teleconnection is a combination of a PNA-like (i.e., state-dependent noise of the form of the PNA) due to changes in the background atmospheric state and a non-PNA (i.e., ENSO signal) or ENSO forced component.

We also addressed here whether there is any relationship between PNA-related noise amplitude and ENSO? For this, we compute the noise EOF as in Fig. 8c but for the El Niño, La Niña, and Neutral years separately using the HRIE noise-reduced simulation. From Fig. 10, we can observe that the spatial distribution and amplitude of the dominant noise pattern is very similar and independent of the state of ENSO, which suggest that mid-latitude noise is, at least

that associate with the PNA, mostly state independent with respect to tropical SST forcing. Also, and as was shown in Fig. 8c, the dominant noise pattern is that of the PNA with about 36% of total noise variance explained. Note that the analysis of Fig. 10 does not address the state-dependent component of the PNA with respect to ENSO. We will discuss this issue later in the manuscript.

To further demonstrate how midlatitude internal variability masks the ENSO-forced response, we calculate the three-dimensional Rossby wave flux for HRCTL and HRIE models during El Niño events. This is shown in Fig. 11a for HRCTL and Fig. 11b for HRIE. The 200 hPa streamfunction is depicted by black contour; horizontal (vertical) wave flux is shown as vectors (shaded) contour. We assume that wave flux associated with ENSO-forced response is considerably smaller than that associated with internal atmospheric variability since the forced ENSO response is so much smaller. Most of the horizontal wave flux is zonally oriented for the HRCTL (Fig. 11a), and dominated by internal atmospheric variability. There is significant wave flux towards the southern and eastern United States associated with ENSO-forcing in HRIE case (Fig. 11b). This is consistent with that of observed ENSO response (Fig. 3) in that significant meridional wave flux from the tropical eastern Pacific that extends towards southwestern United States is observed, which is associated with a cyclonic pattern extends from the eastern North Pacific towards the southern United States.

Recall that Fig. 9 suggests that the systematic differences between HRCTL and HRIE shown in Figs. 8a and 8b and now Figs. 11a and 11b are not due to the reduced sample size of HRCTL, but something more fundamental in the HRIE run. It is hypothesized that even though smaller, the SSTA in HRIE is steadier (less noisy) compared to HRCTL. This would lead to a steadier wave flux, which leads to a more systematic remote response. In order to show this,

23

Fig. 12 depicts composite evolution of SSTA (°C) during the 10 El Niño events for HRCTL a), HRIE b), and cross-equatorial SSTA structure at zero-lag c). Similarly, standard deviation among events (°C) is shown for HRCTL d), HRIE e), and f). Signal-to-noise ratio is described for HRCTL g), HRIE h), and i), where this is defined by the ratio of the magnitude of composite SSTA over the standard deviation among events (i.e., event spread). Both models show similar spatiotemporal SSTA evolution with HRCTL having significantly larger amplitude (Fig. 10a compared to 10b) mostly over the eastern Pacific (Fig. 12c). This is due to more atmospheric noise in the HRCTL simulation compared to the noise reduced HRIE simulation. Internal ocean SST variations should be similar between these model runs as they share the same ocean dynamics. The spread, as measure by the standard deviation among events, is also significantly larger in HRCTL compared to HRIE (Figs. 12d and 12e, respectively). As expected, the signal-to-noise ratio is largest during boreal winter and over the central Pacific for both models. One important distinction is the considerably higher SNR over the eastern Pacific (e.g., east of 160°W, Fig. 12i) for the HRIE case. This implies that SSTA there is steadier, producing a more systematic wave flux and teleconnection as shown earlier compared to HRCTL.

We have shown that noise reduction decreases the amplitude of SSTA and variances, which is supported by results from Lopez and Kirtman 2015 at coarser resolution. This suggests that ENSO is noise-driven and the importance of the noise increases with increasing horizontal model resolution. But we also showed that the PNA is still present in the noise-reduced simulation and this is because it is partially independent of the SST forcing. ENSO forcing of the PNA and teleconnection in general may be different because the SST patterns are different (e.g., smaller amplitude and more coherent or less inter-event differences) in the reduced noise experiment.

The amplitude of the SSTA, to a first order approximation, is what determines the strength of anomalous convection in the tropics, which ultimately affects the amplitude of Rossby wave source term (i.e., planetary vorticity advection by upper level divergent winds). However, this raises an interesting question: how is it possible that the weaker SSTA variance in the HRIE experiment provides a more robust ENSO teleconnection when compared to observations or the HRCTL? The answer is simply that the noise in HRIE is reduced more than the signal, and thus the SNR increases in the ensemble mean response.

5. Asymmetry - Teleconnection

ENSO asymmetry, both in term of its tropical and mid-latitude imprint has been extensively studied (Hoeriling et al., 2001; Manahan and Dai, 2004; An and Jin, 2004; Wu et al., 2005; Zhang et al., 2011; Zhang et al., 2014). The amplitude of the mid-latitude asymmetry in ENSO response is as large as the symmetric response (Zhang et al., 2014) and a key element in the asymmetry is in the surface temperature response. The main scope of this section is to further investigate the asymmetric response to tropical heating associated with ENSO and the potential role of atmospheric internal variability. Here, we analyze the upper troposphere anomalous divergence and geopotential height anomaly during El Niño and La Niña events from observational estimates and the model experiments described earlier. Recall that ENSO asymmetry in term of SSTA and atmospheric Rossby wave forcing (Figs. 4 and 5) goes from highest to lowest for the observed, HRCTL, and HRIE experiment in that order.

Divergence in the tropical upper troposphere is an important parameter to analyze as is one of the main contributors of planetary Rossby wave forcing and teleconnections. Figure 13 shows the observed, HRCTL, and HRIE symmetric and asymmetric components of the 200 hPa anomalous divergence meridionally averaged (5°S to 5°N) across the Pacific Ocean, which is a

main forcing of Rossby wave response through planetary vorticity advection. The analysis of HRIE simulation is performed on the ensemble mean from the 10 atmospheric realizations. The symmetric component is mostly positive with maximum amplitude over the central Pacific associated with anomalous deep convection for the observed and the two simulations. The HRCTL (Fig. 13b) simulation has a stronger symmetric anomaly over the western Pacific than that of observed or HRIE. This is consistent with the westward-extended SSTA (Fig. 4c). The amplitude of the symmetric component of upper level divergence for HRIE is similar to that of observed and HRCTL despite a reduction in SSTA in HRIE (Fig. 4e). This has important implications and supports the argument from the previous section that the HRIE is able to separate ENSO forced response from internal atmospheric noise.

The zonal structure of the asymmetric component is similar for all three cases, with negative (positive) anomaly over the western (central-eastern) Pacific. Comparing asymmetries among the three cases is important, but more so, is to compare the amplitude of the asymmetry with respect to the symmetric component. We point out that for the observed (Fig. 13a), the asymmetric component is positive and significantly larger than the symmetric over the eastern Pacific. For the simulations, the symmetry and asymmetry are comparable for HRCTL over the central Pacific, whereas for HRIE the symmetric component is significantly larger than the asymmetric component. As suggested in Lopez and Kirtman (2015), atmospheric internal variability is an important source for ENSO asymmetry, which leads to asymmetric response shown in Fig. 13.

What is the consequence of asymmetric tropical heating and upper level response in term of mid-latitude circulation over the Pacific-North American sector? To answer this question, Fig. 14 shows the composite of the 200 hPa streamfunction anomaly for boreal winters (DJF)

during El Niño and La Niña events. Note that the asymmetry in ENSO response is largest (smallest) for observed (HRIE) case, consistent with asymmetry in SSTA, Rossby wave source, and tropical upper level divergence (Figs. 4, 5, and 11). The ENSO forced response, with reduced atmospheric noise, is mostly meridionally oriented and highly symmetric (Figs. 14e and 14f). In contrast, the presence of atmospheric internal variability (e.g., observed and HRCTL), introduce asymmetry and more zonal structure.

To analyze ENSO asymmetry and its influence on the state-dependence of the PNA on ENSO, we have calculated the PDF of the PNA index for years during positive, negative, and neutral ENSO conditions as defined by the Niño3.4 index terciles. This was done for the HRIE case as it provides multiple PNA indices for a given ENSO state (one for each ensemble member). The results are shown in Fig. 15 for the ensemble mean, ensemble spread, and signal-to-noise ratio (SNR) of the PNA index. In order to quantify a robust PDF, we subsampled the HRIE experiment by selecting only 6 out 10 ensemble members for each ENSO and non-ENSO year and computed their PDF by repeating the sampling randomly 1000 times with replacement (i.e., an ensemble member can be selected more than once).

The ensemble mean PNA index (i.e., noise dependent component) is rarely positive (negative) during La Niña (El Niño) years (Fig. 15a). Thus, the ensemble mean PDF can be viewed as the state-dependent component of the PNA (i.e., dependent on the state of ENSO). If we look at the ensemble spread (Fig. 15b), El Niño years have more uncertainty in the amplitude of the PNA index when compared to neutral and La Niña years. This is probably caused by the non-linear response of the atmospheric circulation to SST anomalies as well as the smaller SNR of SST anomalies during El Niño years (Fig. 16). Also note that the ensemble spread is significantly larger than the ensemble mean anomalies (Figs. 15a and 15b) regardless of the state

of ENSO. This is easily seen by the small SNR (on the order of 0.55-0.7, Fig. 15c). Interestingly, La Niña years have a higher SNR of the PNA index, owing to the large ensemble mean anomaly (Fig. 15a) and relatively smaller ensemble spread when compared to El Niño years (Fig. 15b). In all, there is substantial change in the SNR of the PNA index associated with the state of ENSO, but more so for La Niña case where the SNR increases significantly.

We also look at inter-event asymmetry (i.e., how different are El Niño event from other El Niño events and similarly how different are La Niña events) to investigate why the smaller SNR of the PNA during El Niño compared to La Niña years. Fig. 16 shows the signal, noise, and SNR for El Niño and La Niña separately in terms of their SST anomalies. Note that both the El Niño signal and noise are larger in amplitude compared to La Niña signal and noise respectively. However, the SNR is considerably smaller for El Niño compared to La Niña. The SNR looks like the signal itself for La Niña, whereas the SNR for El Niño cases is relatively small in the Eastern Pacific east of 140°W. Recall that most of the atmospheric wave activity flux associated with ENSO teleconnection is originated east of 140W (see Fig. 11). Therefore, a small SNR due to large SST inter-event spread in the Eastern Pacific will lead to large spread in teleconnection patterns, thus producing larger SNR in the PNA index during El Niño years as oppose to the La Niña years (Fig. 15c). This inter-event asymmetry in SST anomalies over the Easter Pacific is especially large for the decay phase of El Niño in boreal spring, leading to uncertainties in ENSO impacts over North America (Lee et al. 2014).

6. North American Precipitation Response: ENSO Versus PNA

It was highly anticipated that the extremely warm SSTA during the 2015-16 El Niño event could end the most severe multi-year (2012-2015) drought ever recorded in the state of California (Griffin and Anchukaitis, 2014; Diaz and Wahl, 2015; Seager et al., 2015). However,

California only experienced moderate above-normal rainfall mostly in the northern region during the 2015-16 (Lee et al., 2018). This is contrary to the conventional wisdom that the El Niño phase is associated with enhanced winter precipitation over the southwestern US (Mo, 2010; Lee et al,. 2014b; Hoell et al., 2016), where these precipitation changes are associated with southward and eastward displacement of the jet stream and storm track (Hoeling and Ting, 1994; Tremberth and Hurrel, 1994; Orlanski, 2005; Eicheler and Higgins, 2006). Similarly, it is generally accepted that the La Niña phase tends to increase the likelihood for extreme droughts affecting the southwestern United States (Herweijer et al., 2006; Cook et al., 2007).

The previous sections showed that the upper level atmospheric circulation response to tropical Pacific heating contains a component that is quite distinct and much smaller in amplitude than those from internally generated PNA-like pattern. This was demonstrated by applying statistical analysis to observational data and further validated by numerical modeling experiments where the atmosphere internal variability is suppressed. Now that this distinction was established, we can extend our analysis to precipitation over the US and its influence by ENSO-forced versus internal atmospheric dynamics associated with the PNA. This will help clarify, to some extent, the lack of precipitation signal over the southwestern US during major El Niño events, such as the 2015-16 case.

Figure 17a depicts a scatter diagram of the normalized Niño3.4 and PNA observed indices for DJF, the color coding indicates the observed standardized precipitation anomaly for California during DJF. The three strongest El Niño events of 1982-83, 1997-98, and 2015-16 are also shown. The standardized precipitation anomaly for California was created based on National Weather Service forecasting regions for the state. These regions are delimited so that locations within a given region share a common climate. We quantified a precipitation index for each

29

region, then we normalize these indices by their regional precipitation standard deviation. Finally, we average all normalized regional indices to obtain a state-level index. This methodology ensures that all of the regions in California are weighted equally, although for hydrological planning, it is best to include the physical dimensions in these results rather than the standardize fields.

We note that different ENSO types have distinct teleconnection patterns and thus they produce different precipitation patterns over California as was shown in recent studies (Infanti et al., 2016, Lee et al., 2018), where only events with large SST anomalies in the far eastern Pacific that persists throughout the boreal winter and spring have large influence on rainfall throughout the state of California. Consistent with previous studies, above normal precipitation (e.g., *P*>0.5) is present only when Niño3.4 index is positive. But perhaps more interesting is that, during positive Niño3.4, precipitation anomalies generally decrease when the PNA index is large. For example, both the PNA and Niño3.4 were the largest on record during 2015-16 but California experienced near-normal rainfall. The PNA, or some other teleconnection pattern with an influence on the eastern Pacific storm track, can mask the ENSO-forced response. Also, most of these mid-latitude patterns are of very high amplitude in term of geopotential anomaly, thus serving as the main control of circulation anomalies over the US. This brings a very difficult task in term of subseasonal-to-seasonal predictions as these patterns are highly unpredictable and too strongly reliant on initial conditions, an information that is quickly lost in the atmosphere and makes it difficult to link the weather and climate timescales.

Figure 17 also shows the partial correlation of observed precipitation over North America with Niño3.4 SSTA (Fig. 17b) and PNAindex during boreal winter (Fig. 17c). Partial correlation is an alternative technique to ordinary correlation in that it is of most use when variables (e.g.,

Niño3.4 and PNA index) are highly correlated, as is the case here. This technique is used to separate the effect of each index on the dependent variable with the influence of the remaining or other indices held constant. The dependent variable in this case is precipitation over North America. Significant positive correlation for precipitation is depicted over the southern United States for ENSO winters (Fig. 17b). This is in agreement with 200 hPa circulation pattern presented in Fig. 3b in that the anomalous southward shift in the westerlies bring moist air from the eastern Pacific towards the southwestern United States. The observed precipitation pattern associated with the PNA (Fig. 17c) is significantly distinct from that of ENSO. There is significant anti-correlation (i.e., $r > 0.24$ at 95% confidence level) over the southeastern and western United States, which is opposite of that associated with ENSO. Drier conditions over the southern United States associated with positive PNA are related to the northerly wind anomalies due to the presence of cyclonic (anticyclonic) circulation over the eastern (western) North America. The correlation values in Fig. 17 are borderline significant but we have to keep in mind that these are partial correlation and not Pearson correlation where the later tends to be higher by definition if the supposedly independent indices are correlated (i.e., ENSO and PNA), which they are. We also want to note that the magnitude of the correlation between precipitation and the PNA index is not significantly different than the correlation between precipitation and ENSO for the western US, especially if one excludes the larger El Niño events (not shown).

As previously mentioned, interpreting the remote ENSO forced response is difficult due to the presence of internal atmospheric variability. From Figs. 17b and 17c, we observe that precipitation associated with ENSO forced response is for the most part out-of-phase with that associated with internal variability of the form of the PNA pattern. We further validate this by analyzing precipitation over North America from the two couple model runs described in the

previous sections. Figures 17d and 17e show the partial correlation of precipitation anomaly with Niño3.4 for the HRCTL (control) and HRIE (noise reduced) simulations respectively. Correlation pattern for the HRIE closely match those shown in Fig. 17b. Precipitation pattern for HRCTL (Fig. 17d) case is considerably weaker, with positive correlation near the Atlantic and Pacific coast only. The interior southeastern and southwestern USA present negative correlation, this is due to interference of internal atmospheric variability in this case. These precipitation patterns are in agreement with upper atmosphere circulation structure presented in Fig. 8. Overall, HRIE has a better representation of the observed relationship between precipitation over North America in association with ENSO than that of HRCTL model. This is due to the presence of atmospheric internal variability in the HRCTL, the amplitude of which proved to be almost an order of magnitude larger than the mid-latitude ENSO-forced response. This result suggests that the PNA has significant state-independent (i.e., internal atmosphere variability) component. We are not arguing that ENSO is not a potential driver of the PNA (e.g., state-dependent component), but this is considerably a smaller fraction. This can be further addressed by the composite analysis shown in Fig. 7. There, each ensemble member has the same SST anomaly forcing but produces completely distinct mid-latitude 200 hPa streamfunction anomalies compared to other ensembles, even while having very similar tropical 200 hPa streamfunction anomalies.

Note that the very strong ENSO events (Niño3.4 > 1 standard deviation) is predominantly accompanied by PNA of the same sign. But the correlation between the Niño3.4 index and the PNA index is relatively weak (0.33 for observations, 0.48 for HRCTL, and 0.35 for HRIE), so there is significant PNA variability that cannot be explained by ENSO. This suggests that the PNA can be viewed as a combination of state-independent (internal atmosphere) component and

state-dependent (ENSO or other SST-type of forcing) component, with the earlier being dominant. To complicate matters more, ENSO teleconnections to North America appears to have a component distinct from the PNA (as shown in Figs. 8b and 11b). Therefore, the ENSO-PNA teleconnections towards North America comprises of a deterministic (i.e., ENSO-driven signal as in Fig. 8b which is smaller but a source of seasonal predictability), a state-dependent PNA (i.e., ENSO driven PNA component as in the E-panels in Fig. 7), and a state-independent (i.e., internal atmospheric driven PNA as in Fig. 8c, which is large but highly unpredictable) component.

7. Summary and Discussion

This study analyzes the distinction between ENSO forced and internally generated upper atmospheric circulation pattern and associated precipitation over the Pacific North American sector. This problem has experienced significant debate for the past two decades. The main question we were trying to answer is whether ENSO forces an independent teleconnection pattern, distinct from that associated with the so-called PNA pattern. Or, does it just help amplify the internally generated pattern. Or, does ENSO force two basic teleconnection patterns, such that the resulting ENSO-forced pattern is a blend of a PNA and a non-PNA teleconnection pattern? The answer is the later, the mid-latitude ENSO forced response is a combination of a PNA-like and a non-PNA-like teleconnection pattern. We based our analysis on seasonal mean (i.e., boreal winter) anomalous circulation separated by forced and internally generated components. One main difficulty is that both, ENSO and the PNA present similar seasonal evolution, but are due to different processes. ENSO and associated circulation peaks during early boreal winter. Its mid-latitude response follows quickly (e.g., one-month lag), or more precisely during DJF. On the other hand, the PNA also peaks during DJF and is associated with non-linear wave-mean flow interaction near the jet stream.

We showed that ENSO forced response is masked by atmospheric internal variability, with the latter being 3 to 10 times larger in amplitude. Using statistical analysis of observation and couple model experiments, it was showed that the non-PNA ENSO response presents a meridional structure in streamfunction associated with significant poleward Rossby wave flux emanating mostly from the eastern Pacific. In contrast, the PNA teleconnection pattern is zonally oriented, with most of the wave flux in the zonal direction from the subtropical Pacific towards North America.

We also found that the mid-latitude ENSO forced response is asymmetric between warm and cold events. The response associated with La Niña phase is more similar to that of the negative PNA pattern. The El Niño response, however, is more meridionally oriented, with cyclonic circulation over the eastern Pacific southern USA. This asymmetry is caused by asymmetric ENSO forcing over the tropical Pacific. Upper level divergence and circulation over the tropics during warm events is significantly different to that during cold ENSO seasons. This asymmetry in ENSO response is strongly dependent on the presence of atmospheric internal variability or noise. A noise-reduced coupled model experiment suggested that upper troposphere teleconnection pattern associated with ENSO forcing is symmetric and mostly meridionally oriented in the absence of atmospheric noise. That is, the El Niño forced response is characterized by anomalous high-low-high geopotential height pattern extending from the tropical Pacific towards northern Canada. Similar structure but with reverse sign is associated with La Niña phase.

Over the tropics, SSTA associated with El Niño in the eastern Pacific is significantly more regular (e.g., less noise) when atmospheric noise is reduced. Lopez and Kirtman (2015) found that noise in the zonal wind stress over the eastern Pacific is mostly state independent. The

IE technique is more efficient in reducing this type of noise compared to a state-dependent noise. As a result, the ENSO signal is also damped. On the other hand, reduction in SSTA noise over the eastern Pacific produces a more systematic heating, hence steadier wave flux. This leads to more systematic teleconnection pattern.

Over midlatitude PNA region, 200 hPa geopotential height anomalies associated with ENSO have smaller signal-to-noise ratio in the noise-reduced experiment compared to the control case. This is a consequence of reduced tropical SSTA forcing due to noise filtering, while internal atmospheric noise at 200 hPa is comparable in both cases. The HRIE run allows for distinguishing between forced versus internally generated patterns via multiple atmosphere ensemble realization. We found that longer control simulations will not be enough to separate these patterns given the presence of inter-event ENSO asymmetry due to state independent noise (i.e., the type of noise that is independent of SST forcing and thus filtered by the IE technique) forcing over the eastern Pacific. This is consistent with Lopez and Kirtman 2015, which found that state-independent noise is responsible for most of the ENSO phase asymmetry (i.e., differences between El Niño and La Niña) and for most of the ENSO diversity (i.e., different among El Niño events).

This study also looked at precipitation patterns over North America and the influence of internal atmospheric variability. There is significant correlation of the Niño3.4 SST anomaly and precipitation over the southern USA and northern Mexico extending from the Pacific to the Atlantic coast. But the ENSO-US precipitation relationship is strongly influenced by the presence of large internal atmospheric variability, dominated by the PNA pattern. The enhanced precipitation over the southern and western US during El Niño events can be explained as in Seager et al. (2005a) due to eddy-forced ascent and tropospheric cooling in midlatitudes. This

eddy-forced ascent is caused by southward shift of the mean flow in the subtropics due to thermal wind balance in response to enhanced meridional temperature gradient over the subtropics. The southward shift of the mean flow causes eddy momentum flux divergence, this must be balanced by equatorward flow at upper levels producing anomalous ascent and precipitation over midlatitudes. We suggest that the presence of internal variability such as the PNA, may weaken or amplify the ENSO signal depending on the phase or form of internal atmospheric noise. For example, during positive PNA, anticyclonic circulation over western North America can shift the subtropical jet stream north, competing with the southward shift in the jet associated with ENSO-like warming. This could be the reason why the precipitation pattern associated with ENSO over the southern US is more systematically represented by the noise-reduced model compare to the control model.

While the PNA is largely viewed as an internal atmospheric mode of variability, it contains a significant state-dependent component which is dependent on the state of ENSO, where a positive (negative) PNA is more likely during El Niño (La Niña) winters. Although, this state-dependent component is found to be considerably smaller than the state-independent component, leading to low SNR of the PNA. We also found a state-dependence in the SNR of the PNA with smaller SNR during El Niño winters compared to La Niña winters, which could have repercussions on ENSO teleconnections, suggesting that La Niña mid-latitude teleconnections could be more predictable than El Niño teleconnections. But this is beyond the scope of this study and subject to future investigation.

To conclude, the importance of atmospheric internal variability cannot be underestimated. From the perspective of the general circulation, this noise appears to play a fundamental role in diversifying both, ENSO forcing and response with significant social and

economic footprint. For example, the large 2015-16 El Niño was anticipated to alleviate the persistent drought that affected the western US. This did not occur, as this study suggests, due to the presence of a strong positive PNA pattern. The reason is that the ENSO composite using historical records includes a substantial PNA component, so the winter forecast for North America basically always has a substantial PNA component in it when influenced by the historical composite. The forecast bust comes when the actual circulation response doesn't look like the composite (e.g., the case for 2015-16, and again for 2016-17). However, we are not suggesting here that a better forecast of wintertime climate anomalies should exclude the influence of internal variability like the PNA. What we are trying to convey is that the ENSO teleconnection pattern is masked by the larger amplitude weather noise, such as the PNA. With that said, a better forecast should make note of such distinction between ENSO and PNA and not just assume that because there is an El Niño event developing, the southwestern US should get a wet winter. This can lead to a forecast "bust" as it occurred with the 2015-16 El Niño event. Further studies on this are needed to fully understand the relative role of forced coupled response and internal atmospheric variability on the climate system.

References

An, S.-I., and F.-F. Jin (2004): Nonlinearity and asymmetry of ENSO. *J. Climate*, 17, 2399–2412.

Andrews, D. G., and M. E. McIntyre (1976): Planetary waves in horizontal and vertical shear: The generalized Eliassen-Palm relation and the mean zonal acceleration. *J. Atmos. Sci.,* 33, 2031–2048.

Barlow, M., S. Nigam, and E. H. Berbery (2001): ENSO, Pacific decadal variability, and U.S. Summertime precipitation, drought, and stream flow. *J. Climate,* 14, 2105–2128.

Barsugli, J. J., and P. D. Sardeshmukh (2002): Global atmospheric sensitivity to tropical SST anomalies throughout the Indo Pacific basin. *J. Climate,* 15, 3427–3442.

Becher, A., and coauthors (2013): A description of the global land-surface precipitation data products of the Global Precipitation Climatology Centre with sampling applications including centennial trend analysis from 1901-present. *Earth Syst. Sci. Data,* 5, 71–99.

Blade, I. (1999): The influence of midlatitude ocean–atmosphere coupling on the low-frequency variability of a GCM. Part II: Interannual variability induced by tropical SST forcing. *J. Climate,* 12, 21–45.

Bryan, F. O., R. Tomas, J. M. Dennis, D. B. Chelton, N. G. Loeb, and J. L. McClean (2010): Frontal-scale air-sea interaction in high-resolution coupled climate models. *J. Climate,* 23, 6277–6291.

Carton, J. A., and B. S. Giese (2008): A reanalysis of ocean climate using simple ocean data assimilation (SODA). *Mon. Wea. Rev*., 136, 2999–3017.

Cook, E. R., R. Seager, M. A. Cane, and D. W. Stahle (2007): North American drought: Reconstruction, causes and consequences. *Earth Sci. Rev.,* 81, 93–134.

Chen, J., A. D. Del Genio, B. E. Carlson, and M. G. Bosilovich (2008): The spatiotemporal structure of twentieth-century climate variations in observations and reanalyses. Part II: Pacific pan-decadal variability. *J. Climate,* 21, 2634–2650.

Danabasoglu, G., and J Marshall (2007): Effects of vertical variations of thickness diffusivity in an ocean general circulation model. *Ocean Modelling*, 18, 122–141.

Danabasoglu, G., S. C. Bates, B. P. Briegleb, S. R. Jayne, M. Jochum, W. G. Large, S. Peacock, and S. G. Yeager (2011): The CCSM4 ocean component. *J. Climate,* 25 (5), 1361–1389.

DeWeaver, E., and S. Nigam (2004): On the forcing of ENSO teleconnections by anomalous heating and cooling. *J. Climate,* 1 (7), 3225–3235.

Delworth, T. L., and coauthors (2012): Simulated climate and climate change in the GFDL CM2.5 high-resolution coupled climate model. *J. Climate*, 25, 2755–2781.

Diaz, H. F., and E. R. Wahl (2015): Recent California water year precipitation deficits: A 440-year perspective. *J. Climate*, 28, 4637–4652.

Eichler, T., and W. Higgins (2006): Climatology and ENSO-related variability of North American extratropical cyclone activity. *J. Climate*, 19, 2076–2093.

Gershunov, A., and T. P. Barnett (1998): Interdecadal modulation of ENSO teleconnections. *Bull. Amer. Meteor. Soc.,* 79, 2715–2725.

Gershunov, A., and D. Cayan (2003): Heavy daily precipitation frequency over the contiguous United States: Sources of climate variability and seasonal predictability. *J. Climate,* 16, 2752–2765.

Griffin, D., and K. J. Anchukaitis (2014): How unusual is the 2012-2014 California drought? *Geophys. Res. Lett.*, 41, 9017–9023.

Hannachi, A., D. Stephenson, and K. Sperber (2003): Probability-based methods for quantifying nonlinearity in the ENSO. *Clim. Dyn.,* 20, 241–256.

Herweijer, C., R. Seager, and E. R. Cook (2006): North American droughts of the mid to late nineteenth century: A history, simulation and implication for Mediaeval drought. *Holocene,* 16 (2), 159–171.

Hoell, A., M. Hoerling, J. Eischeid, K. Wolter, R. Dole, J. Perlwitz, T. Xu, and L. Cheng (2016): Does El Niño intensity matter for California precipitation? *Geophys. Res. Lett*., 43, 819–825.

Hoerling, M. P., and M. Ting (1994): Organization of extratropical transients during El Niño. *J. Climate*, 7, 745–766.

Hoerling, M. P., A. Kumar, and M. Zhong (1997): El Niño, La Niña, and the nonlinearity of their teleconnections. *J. Climate*, 10, 1769–1786.

Hoerling, M., A. Kumar, and T. Xu (2001): Robustness of the nonlinear climate response to ENSO's extreme phases. *J. Climate*, 14, 1277–1293.

Huang, B., P. Thorne, V. Banzon, T. Boyer, G. Chepurin, J. Lawrimore, M. Menne, T. Smith, R. Vose, and H. Zhang (2017): Extended reconstructed sea surface temperature version 5 (ERSSTv5): Upgrades, validations, and Intercomparisons. *J. Climate*, 30, 8179–8205.

Infanti, J. M., and B. P. Kirtman (2016): North American rainfall and temperature prediction response to the diversity of ENSO. *Clim. Dyn.*, 46, 3007–3023.

Jochum, M., G. Danabasoglu, M. Holland, Kwon, and W. Large (2008): Ocean viscosity and climate. *J. Geophys. Res.,* 113, C06017.

Jochum, M. (2009): Impact of latitudinal variations in vertical diffusivity on climate simulations, *J. Geophys. Res.,* 114, C01010.

Kalnay, E., and coauthors (1996): The NCEP/NCAR 40-year reanalysis project. *Bull. Amer. Meteor. Soc.,* 77 (3), 437–471.

Kam, J., J. Sheffield, and E. F. Wood (2014): Changes in drought risk over the contiguous United States (1901-2012): The influence of the Pacific and Atlantic Oceans. *Geophys. Res. Lett.,* 41, 5897–5903.

Karoly, D. J., R. A. Plumb, and M. Ting (1989): Examples of the horizontal propagation of quasi-stationary waves. *J. Atmos. Sci.,* 46, 2802–2811.

Kirtman, B. P., and J. Shukla (2002): Interactive coupled ensemble: A new coupling strategy for GCMs. *Geophys. Res. Lett.,* 29**,** 1029–1032.

Kirtman, B. P., D. M. Straus, D. H. Min, E. K. Schneider, and L. Siqueira (2009): Toward linking weather and climate in the interactive ensemble NCAR climate model. *Geophys. Res. Lett.,* 36 (13), L13705.

Kirtman, P. B., E. K. Schneider, D. M. Straus, D. Min, and R. Burgman (2011): How weather impacts the forced climate response. *Clim. Dyn.,* 37, 2389–2416.

Kirtman, P. B., and coauthors (2012): Impact of ocean model resolution on CCSM climate simulations. *Clim. Dyn.,* 39, 1303–1328.

Kirtman, B. P., N. Perlin, and L. Siqueira (2017): Ocean eddies and climate predictability. *Chaos,* 27 (12), 126902.

Lau, N.-C. (1981): A diagnostic study of recurrent meteorological anomalies appearing in a 15-year simulation with a GFDL general circulation model. *Mon. Wea. Rev.,* 109, 2287–2311.

Lau, N.-C. (1997): Interactions between global SST anomalies and the midlatitude atmospheric circulation. *Bull. Amer. Meteor. Soc.,* 78, 21–33.

Lau, N.-C., and M. J. Nath (1994): A modeling study of the relative roles of tropical and extratropical SST anomalies in the variability of the global atmosphere–ocean system. *J. Climate*, 7, 1184–1207.

Larson, S.*,* and B. Kirtman (2013): The Pacific Meridional Mode as a trigger for ENSO in a high-resolution coupled model. *Geophys. Res. Lett.,* 40*,* 3189–3194*.*

Lee, S.-K., B. E. Mapes, C. Wang, D. B. Enfield, and S. J. Weaver (2014b): Springtime ENSO phase evolution and its relation to rainfall in the continental U.S. *Geophys. Res. Lett*., 41, 1673–1680.

Lee, S.-K., H. Lopez, E.-S. Chung, P. DiNezio, S-W. Yeh, and A.T. Wittenberg (2018): On the fragile relationship between El Niño and California rainfall. *Geophys. Res. Lett.,* 45, 907–915.

Lopez, H., B. P. Kirtman, E. Tziperman, and G. Gebbie (2013): Impact of interactive westerly wind bursts on CCSM3. *Dyn. Atmos. Oceans,* 59, 24–51.

Lopez, H., and B. P. Kirtman (2015): Tropical Pacific internal atmospheric dynamics and resolution in a coupled GCM. *Clim. Dyn.,* 44 (1-2), 509–527.

Lin, Y. H., L. E. Hipps, S. Y. S. Wang, and J. H. Yoon (2017): Empirical and modeling analyses of the circulation influences on California precipitation deficits. *Atmos. Sci. Lett.*, 18 (1), 19–28.

McCabe, G. J., and M. D. Dettinger (1999) Decadal variations in the strength of ENSO teleconnections with precipitation in the western United States. *Internat. J. Climatol.,* 19 (13), 1399–1410.

McClean, J., and coauthors (2011): A prototype two-decade fully-coupled fine-resolution CCSM simulation. *Ocean Modelling*, 39 (1-2), 10–30.

Mo, K. C. (2010): Interdecadal modulation of the impact of ENSO on precipitation and temperature over the United States. *J. Climate*, 23, 3639–3656.

Monahan, A. H., and A. Dai (2004): The spatial and temporal structure of ENSO nonlinearity. *J. Climate*, 17, 3026–3036.

Mantua, N. J., S. R. Hare, Y. Zhang, J. M. Wallace, and R. C. Francis (1997): A Pacific interdecadal climate oscillation with impacts on salmon production. *Bull. Amer. Meteor. Soc.,* 78:1069–1079.

Mantua, N. J., and S. R. Hare (2002): The Pacific decadal oscillator. *J. Oceanogr.,* 58, 35–44.

Molteni, F., L. Ferranti, T. N. Palmer, and P. Viterbo (1993): A dynamical interpretation of the global response to equatorial Pacific SST anomalies. *J. Climate*, 6, 777–795.

Neale, R. B., J. H. Richter, and M. Jochum (2008): The impact of convection on ENSO: From a delayed oscillator to a series of events. *J. Climate*, 21, 5904–5924.

Orlanski, I. (2005). A new look at the Pacific storm track variability: Sensitivity to tropical SSTs and to upstream seeding. *J. Atmos. Sci.*, 62, 1367–1390.

Palmer, T. N. (1999): A nonlinear dynamical perspective on climate prediction. *J. Climate,* 12, 575–591.

Philander, S. G. (1990): *El Niño, La Niña, and the Southern Oscillation*. Academic Press, 293 pp.

Piao, L., Z. Fu, and N. Yuan (2016)" "Intrinsic" correlations and their temporal evolutions between winter-time PNA/EPW and winter drought in the west United States. *Scien. Repts.*, 6, 19958.

Plumb, R. A. (1985): On the three-dimensional propagation of stationary waves. *J. Atmos. Sci.,* 42, 217–229.

Putrasahan, D. A., I. Kamenkovich, M. Le Henaff, and B. P. Kirtman (2017): Importance of ocean mesoscale variability for air-sea interactions in the Gulf of Mexico. *Geophys. Res. Lett*., 44, 6352–6362.

Robeson, S. M. (2015): Revisiting the recent California drought as an extreme value. *Geophys. Res. Lett*., 42, 6771–6779.

Sarachik, E. S., and M. A. Cane (2010): *The El Niño-Southern Oscillation Phenomenon*. Cambridge Univ. Press, Cambridge, United Kingdom.

Schubert, S. D., M. J. Suarez, P. J. Pegion, R. D. Koster, and J. Bacmeister (2004a): Causes of long-term drought in the US Great Plains, *J. Climate*, 17 (3), 485–503.

Schubert, S. D., M. J. Suarez, P. J. Pegion, R. D. Koster, and J. Bacmeister (2004b): On the cause of the 1930s Dust Bowl. *Science*, 303 (5665), 1855–1859.

Seager, R., N. Harnik, W. A. Robinson, Y. Kushnir, M. Ting, H. P. Huang, and J. Velez (2005a): Mechanisms of ENSO-forcing of hemispherically symmetric precipitation variability. *Quart. J. Roy. Meteor. Soc.,* 131, 1501–1527.

Seager, R., Y. Kushnir, C. Herweijer, N. Naik, and J. Velez (2005b): Modeling of tropical forcing of persistent droughts and pluvials over western North America: 1856–2000. *J. Climate*, 18, 4065–4088.

Seager, R., R. Burgman, Y. Kushnir, A. Clement, E. Cook, N. Naik, and J. Miller (2008): Tropical Pacific forcing of North American medieval megadroughts: Testing the concept with an atmosphere model forced by coral reconstructed SSTs. *J. Climate,* 21, 6175–6190.

Seager, R., M. Hoerling, S. Schubert, H. Wang, B. Lyon, A. Kumar, J. Nakamura, and N. Henderson (2015): Causes of the 2011 to 2014 California drought. *J. Climate*, 28, 6997–7024.

Schneider, E. K., and M. Fan (2007): Weather noise forcing of surface climate variability. *J. Atmos. Sci.*, 64, 3265–3280.

Siqueira, L., and B. P. Kirtman (2016): Atlantic near-term climate variability and the role of a resolved Gulf Stream. *Geophys. Res. Lett.*, 43(8), 3964–3972.

Straus, D. M., and J. Shukla (2002): Does ENSO force the PNA? *J. Climate*, 15, 2340–2358.

Trenberth, K. E. (1990): Recent observed interdecadal climate changes in the Northern Hemisphere. *Bull. Amer. Meteor. Soc.*, 71, 988–993.

Trenberth, K. E., and J. W. Hurrell (1994): Decadal atmosphere–ocean variations in the Pacific. *Clim. Dyn.*, 9, 303–319.

Trenberth, K. E., G. W. Branstator, D. Karoly, A. Kumar, N.-C. Lau, and C. Ropelewski (1998): Progress during TOGA in understanding and modeling global teleconnections associated with tropical Pacific sea surface temperatures. *J. Geophys. Res.,* 103, 14,291–14,324.

Wallace, J. M., and D. S. Gutzler (1981): Teleconnections in the geopotential height field during the Northern Hemisphere winter. *Mon. Wea. Rev.,* 109, 784–812.

Wang, H., and S. Schubert (2014): Causes of the extreme dry conditions over California during early 2013. *Bull. Amer. Meteor. Soc.,* 95, S7–S11.

Weng, H., S. Behera, and T. Yamagata (2009): Anomalous winter climate conditions in the Pacific rim during recent El Niño Modoki and El Niño events. *Clim. Dyn*, 32, 663–674.

Westerling, A. L., H. G. Hidalgo, D. R. Cayan, and T. W. Swetnam (2006): Warming and earlier spring increase western US forest wildfire activity. *Science*, 313, 940–943.

Wu, L., Z. Liu, R. Gallimore, R. Jacob, D. Lee, and Y. Zhong (2003): Pacific decadal variability: The tropical Pacific mode and the North Pacific mode. *J. Climate*, 16, 1101–1120.

Wu, R., and B. P. Kirtman (2003): On the impact of the Indian summer monsoon on ENSO in a coupled GCM. *Quart. J. Roy. Meteor. Soc.,* 129, 3439–3468.

Wu, Z., E. K. Schneider, and B. P. Kirtman (2004): Causes of low frequency North Atlantic SST variability in a coupled GCM. *Geophys. Res. Lett.,* 31, L09210.

Wu, A., W. W. Hsieh, and A. Shabbar (2005): The nonlinear patterns of North American winter temperature and precipitation associated with ENSO. *J. Climate*, 18, 1736–1752.

Yeh, S.-W., and B. P. Kirtman (2004a): The impact of atmospheric internal variability on the North Pacific SST variability. *Clim. Dyn*., 22 (6-7), 721–732.

Yu, J.-Y., and Y. Zou (2013): The enhanced drying effect of Central-Pacific El Niño on US winter. *Environ. Res. Lett.*, 8, 014019.

Zhang, T., M. P. Hoerling, J. Perlwitz, D.-Z. Sun, and D. Murray (2011): Physics of U.S. surface temperature response to ENSO. *J. Climate*, 24, 4874–4887.

Zhang, T., J. Perlwitz, and M. P. Hoerling (2014): What is responsible for the strong observed asymmetry in teleconnections between El Niño and La Niña? *Geophys. Res. Lett.,* 41, 1019–1025.

Zhang, Y., Y. Qian, V. Duliere, E. Salathe, and L. Leung (2012): ENSO anomalies over the Western United States: present and future patterns in regional climate simulations. *Clim. Change*, 110, 315–346.
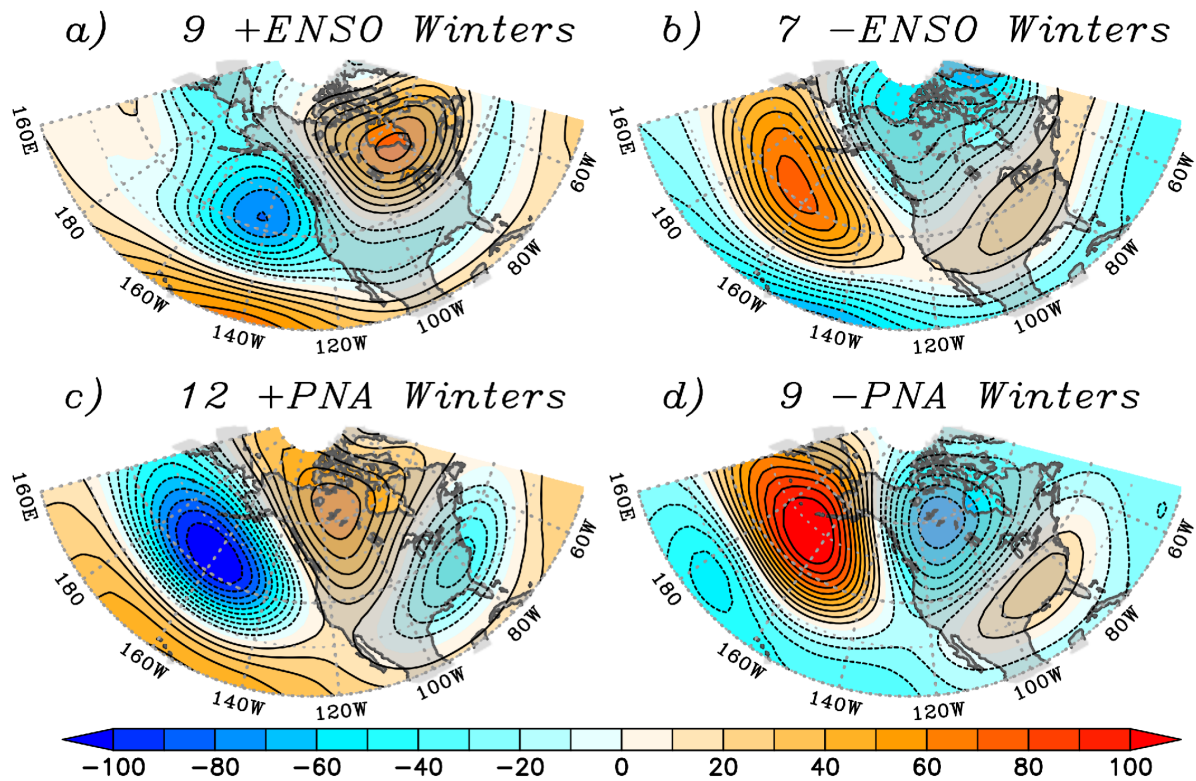
Figure 1. Composite of 200 hPa geopotential height anomaly during DJF for a) warm ENSO events, b) cold ENSO events, c) warm PNA winters, and d) cold PNA winters. Contour interval is 10 m. The number in each subtitle corresponds to the number of events in the composite.
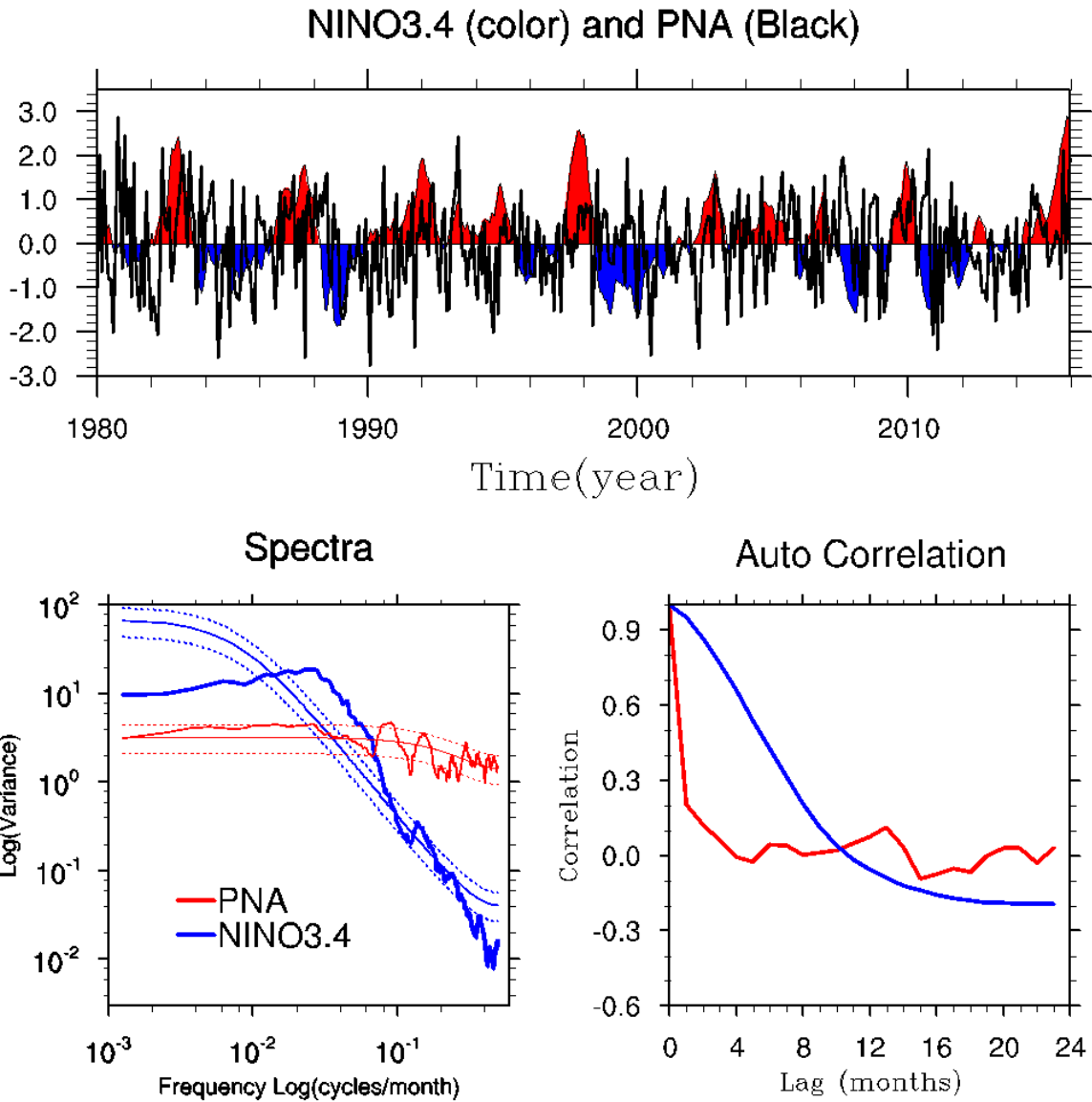
Figure 2. Time series of Niño3.4 SSTA (color) and PNA (black) from January 1980 to December 2016. Lower left panel show the spectral density and lower right panel show the autocorrelation for Niño3.4 (blue) and PNA (red) index.
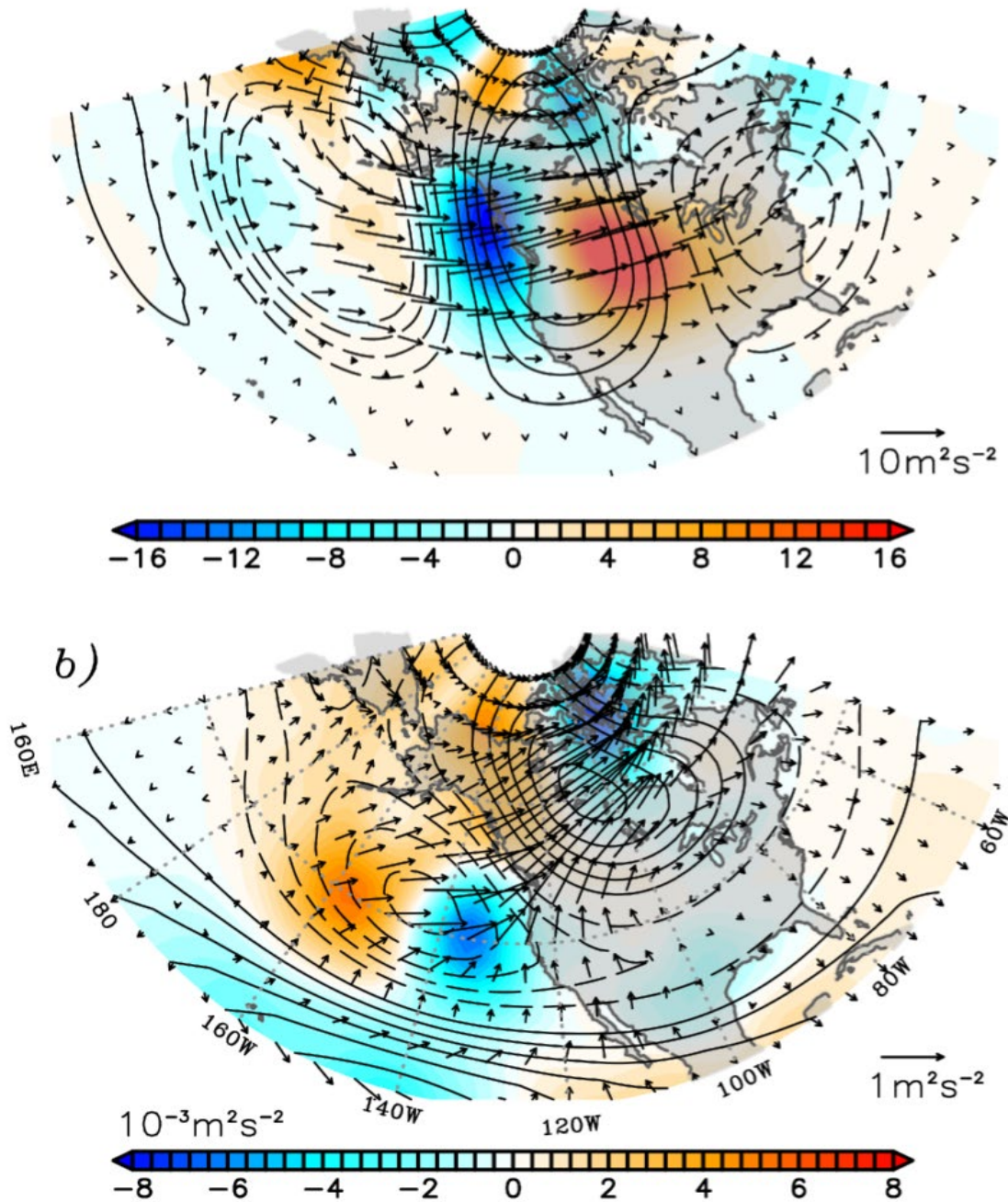
Figure 3. Conditional composite of 200 hPa anomalous streamfunction (contour), horizontal (vector) and vertical (shaded) stationary Rossby wave flux of December-January-February (DJF) seasonal mean during a) positive PNA and neutral ENSO, and b) positive ENSO events and neutral PNA. Streamfunction contour interval is 3 x 10^6 s-1 for panel a) and 10^6 s^{-1} for b).
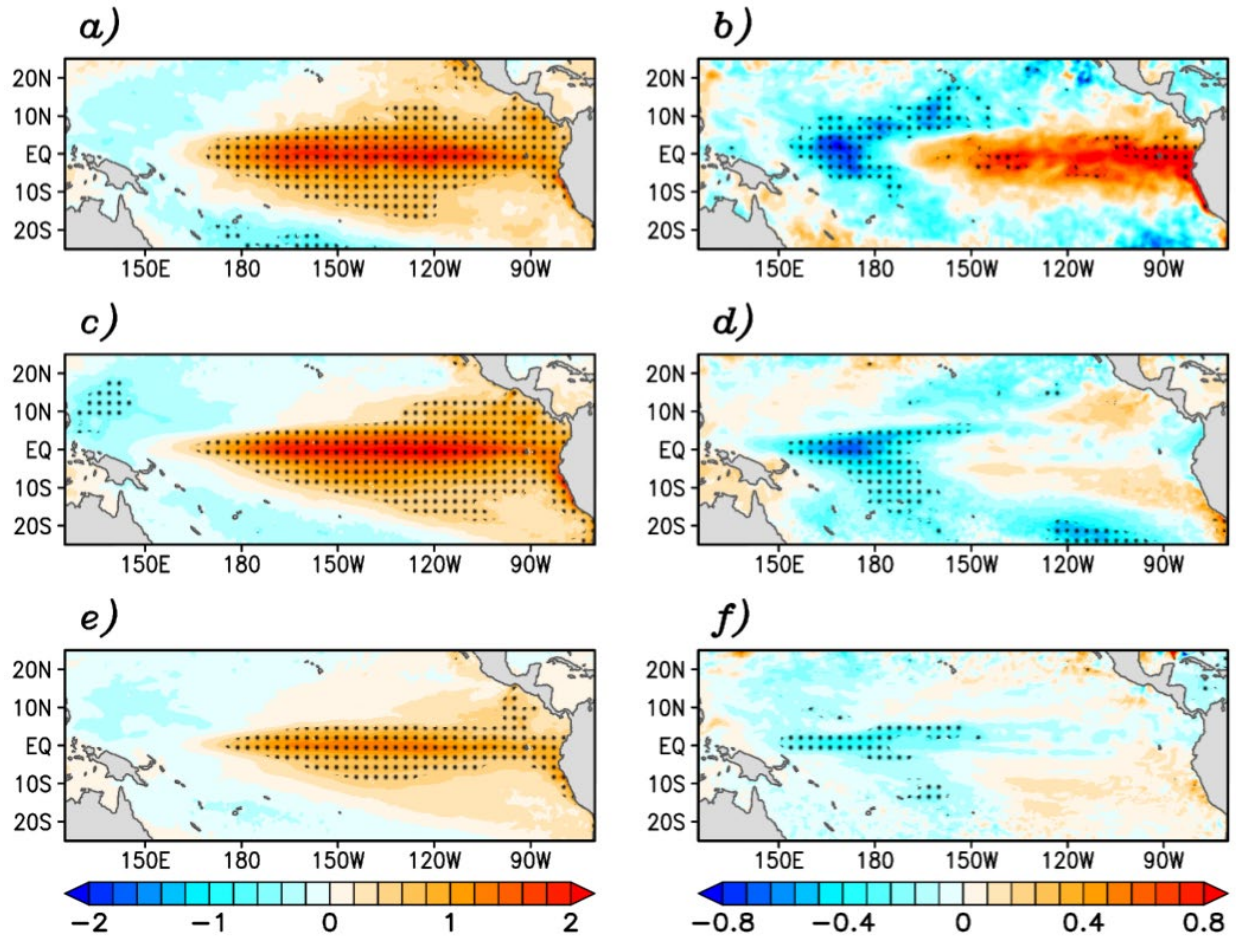
Figure 4. Composite of December-January-February SSTA for symmetric (left-column) and asymmetric (right-column) component of ENSO for observed (a and b), HRCTL (c and d), and HRIE model (e and f) respectively. The symmetric component is defined by warm minus cold events divided by 2, where the asymmetric is warm plus cold events SSTA. Dotted contours indicate statistical significance to 95% based on student-T test.
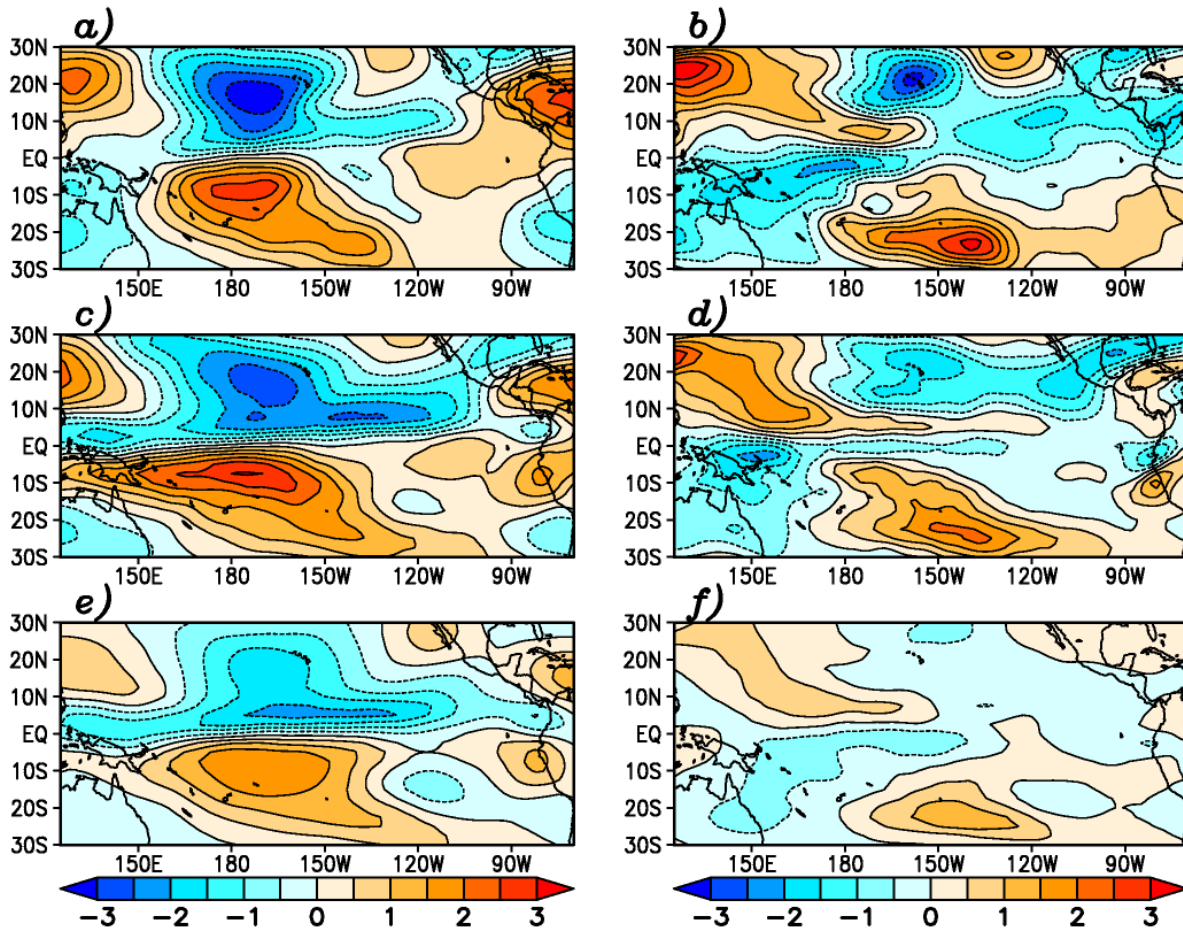
Figure 5. Same as in Fig. 4 but for the Rossby wave source. Contour interval is 0.5 x 10^{-11} s^{-2}. Anticyclonic (cyclonic) wave source is negative (positive) in the Northern Hemisphere and the opposite in the Southern Hemisphere.
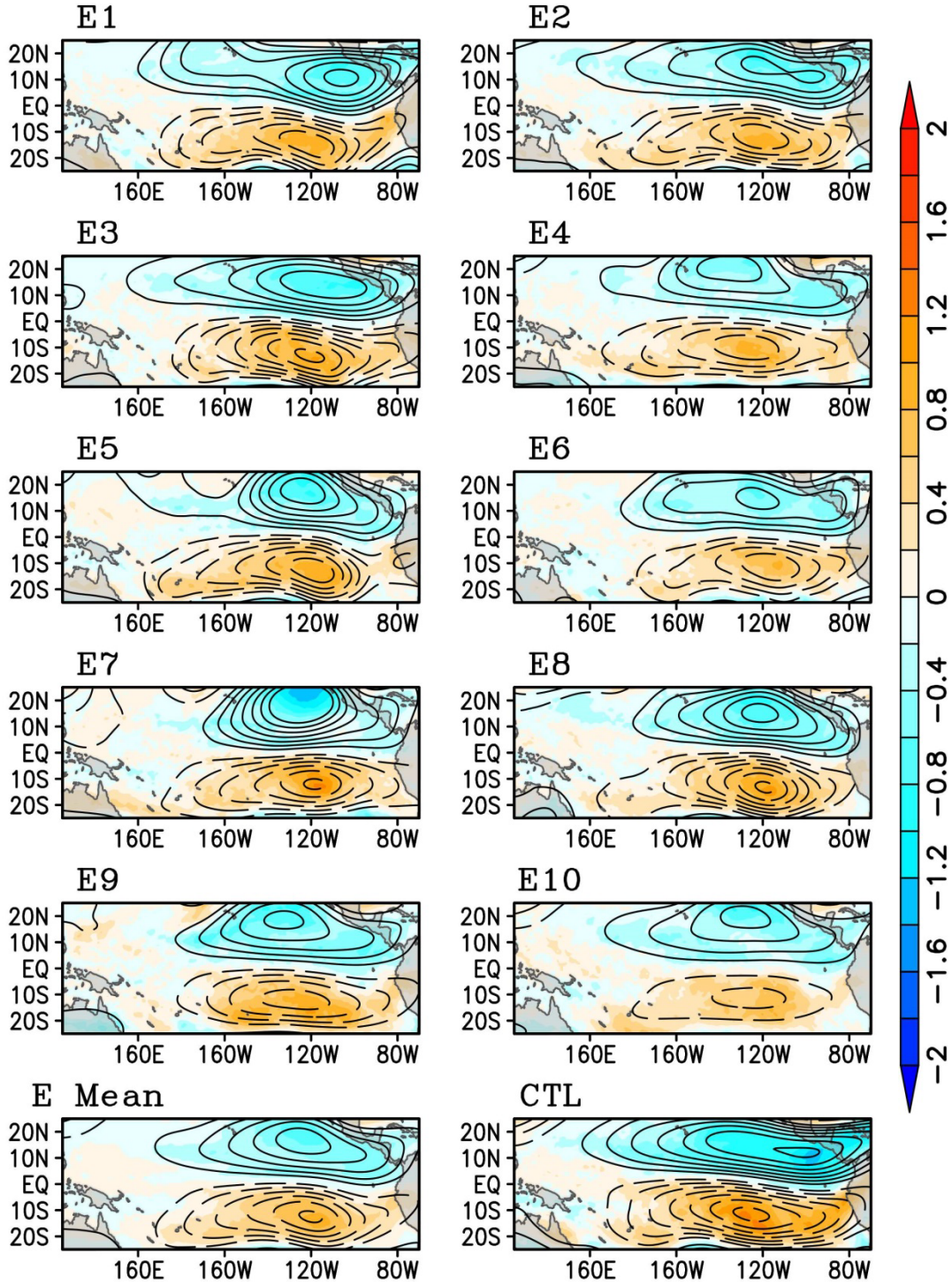
Figure 6. Composite of 200 hPa streamfunction (10^6 s^{-1}, contour) and relative vorticity (10^{-5} s^{-1}, shaded) for warm ENSO events. Panels E1 through E10 correspond to atmospheric members of IE model. Emean panel indicates ensemble mean of IE model, whereas CTL panel corresponds to CTL model. The composite is based on the top 10 El Niño events centered on December-January-February.
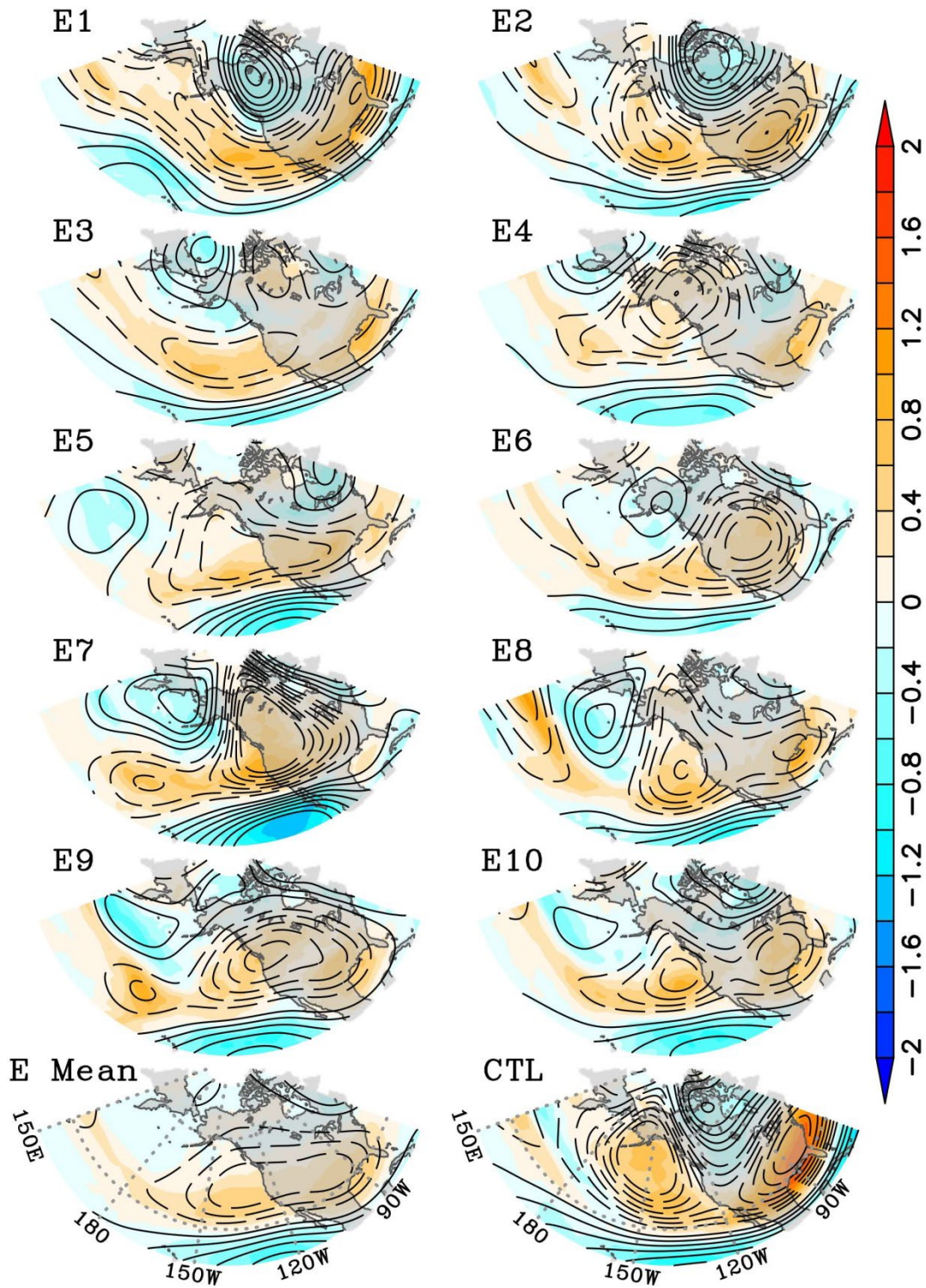
Figure 7. Same as Fig. 6 but for the Pacific-North American sector.
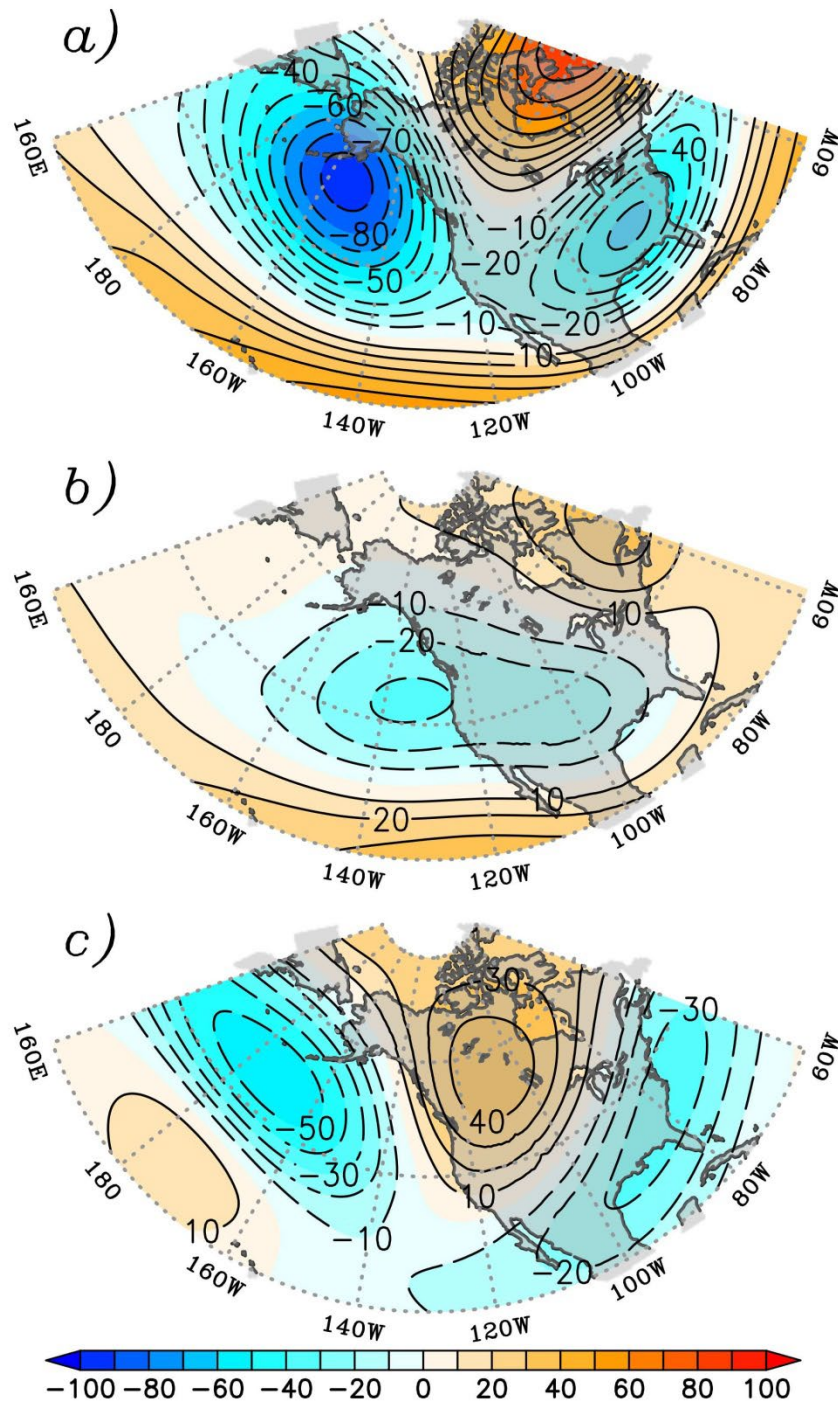
Figure 8. Composite of 200 hPa geopotential height anomaly during DJF for warm ENSO events for HRCTL model a) and HRIE model b). Also showing the spatial structure of EOF 1 of internal atmospheric dynamics 200 hPa geopotential height for HRIE model c). Contour interval is 10 m for all panels.
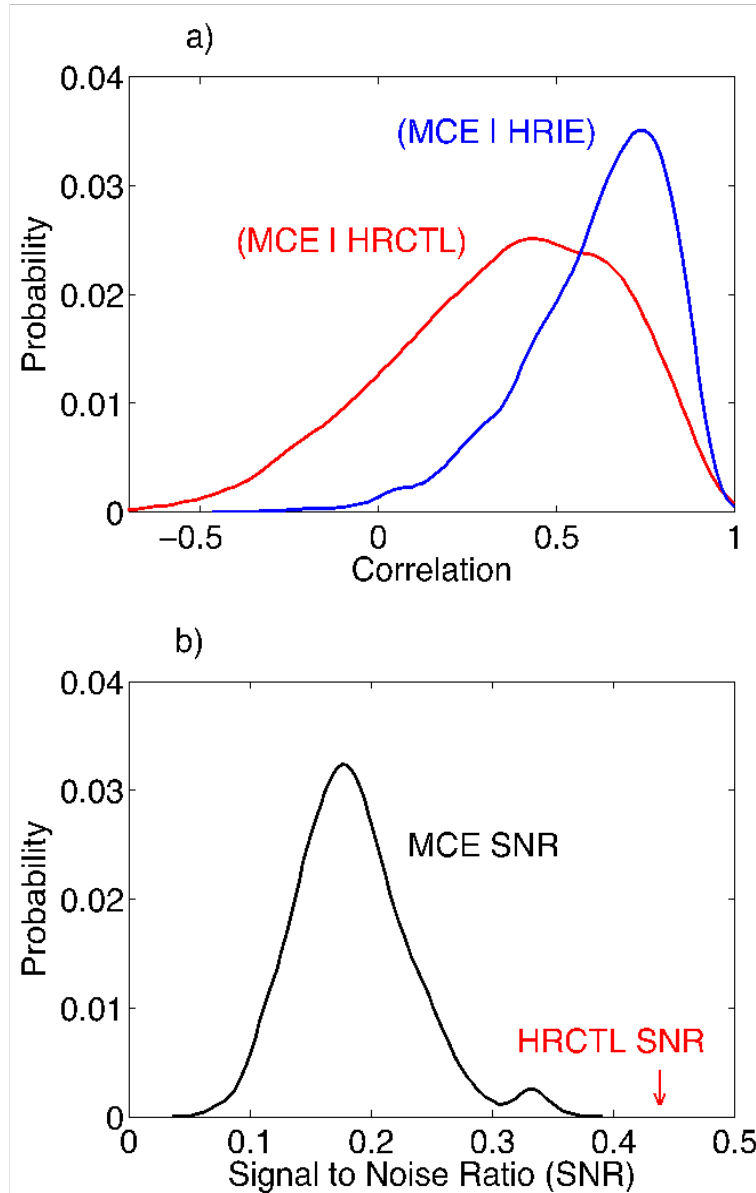
Figure 9. Probability density function (PDF) for the spatial correlation between MCE and HRCTL composite (red) and the spatial correlation of MCE and HRIE composite (blue) of midlatitude 200 hPa geopotential height anomaly during El Niño events a). b) PDF of signal-to-noise ratio (SNR) of MCE composite (black) compared to HRCTL SNR (red arrow). The MCE are built by 5000 realizations using a Monte Carlo sampling technique.
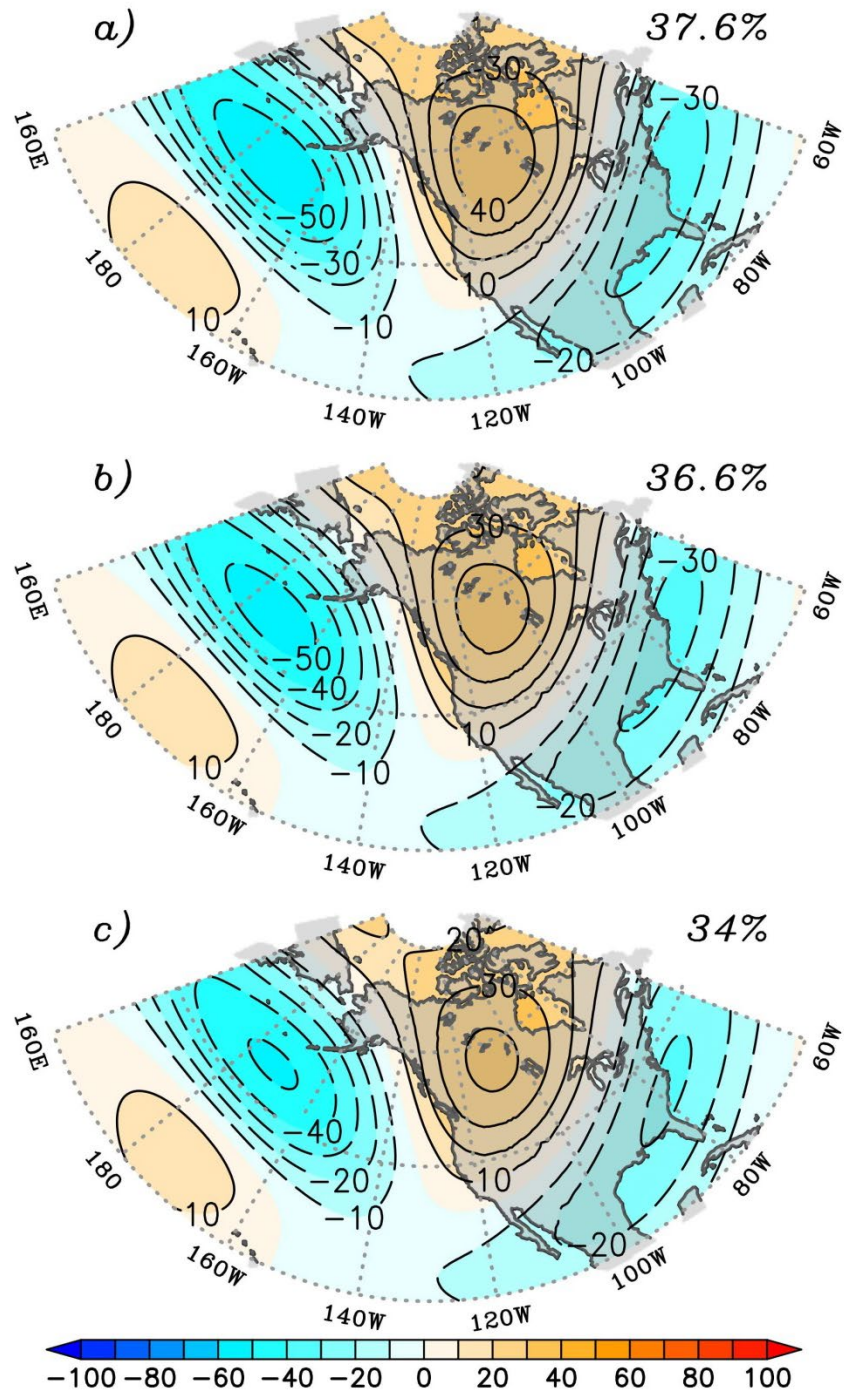
Figure 10. The spatial structure of EOF 1 of internal atmospheric dynamics of 200 hPa geopotential height for HRIE model for; a) El Niño, b) La Niña, and c) Neutral boreal winters. Contour interval is 10m for all panels. The percentage values indicate the variance explained by this EOF 1.

56
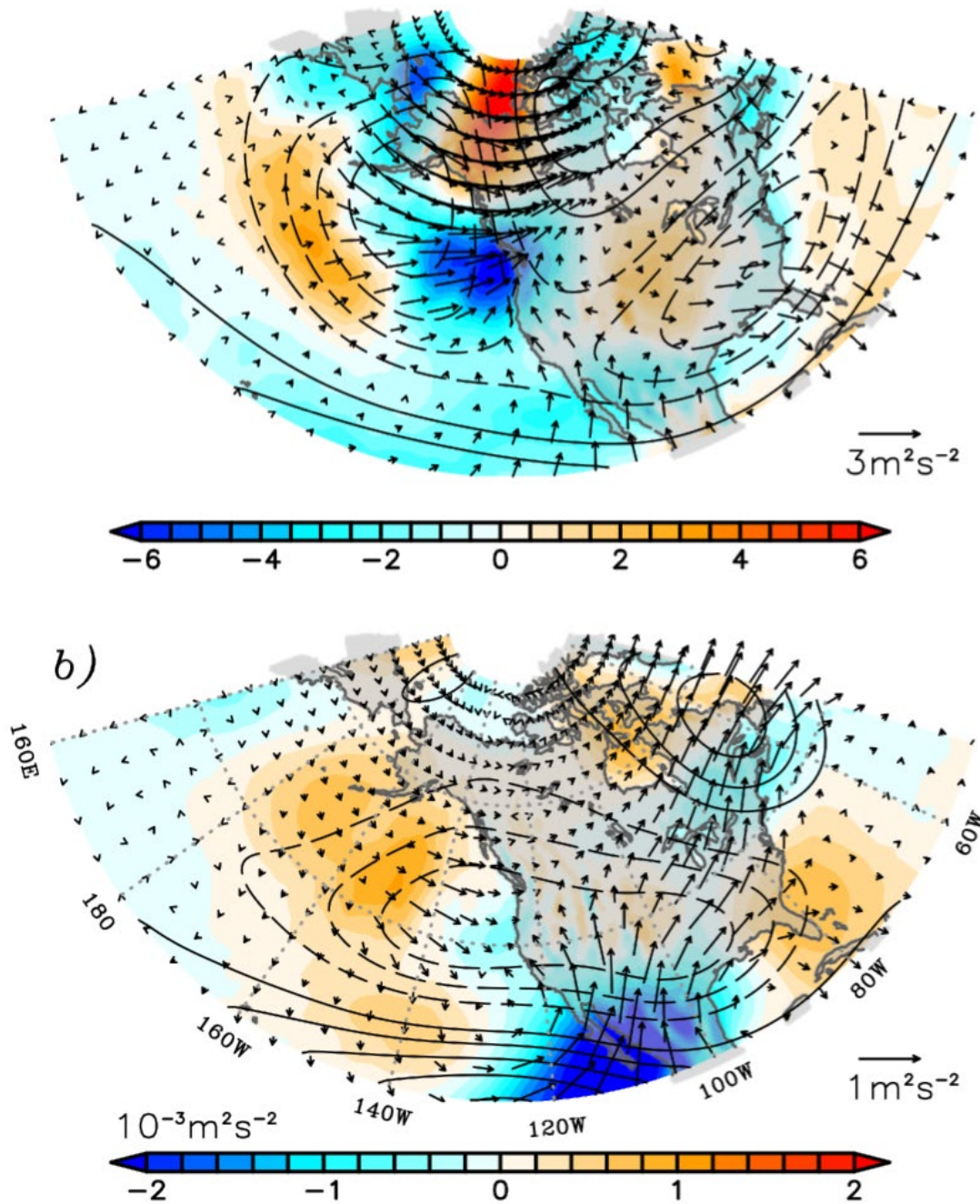
Figure 11. Composite of December-January-February (DJF) seasonal mean 200 hPa anomalous streamfunction (10^6 s^{-1}, contour), horizontal (vector) and vertical (shaded) stationary Rossby wave flux during El Niño events for HRCTL a) and HRIE b). Composite is defined based on the top 10 strongest El Niño events.
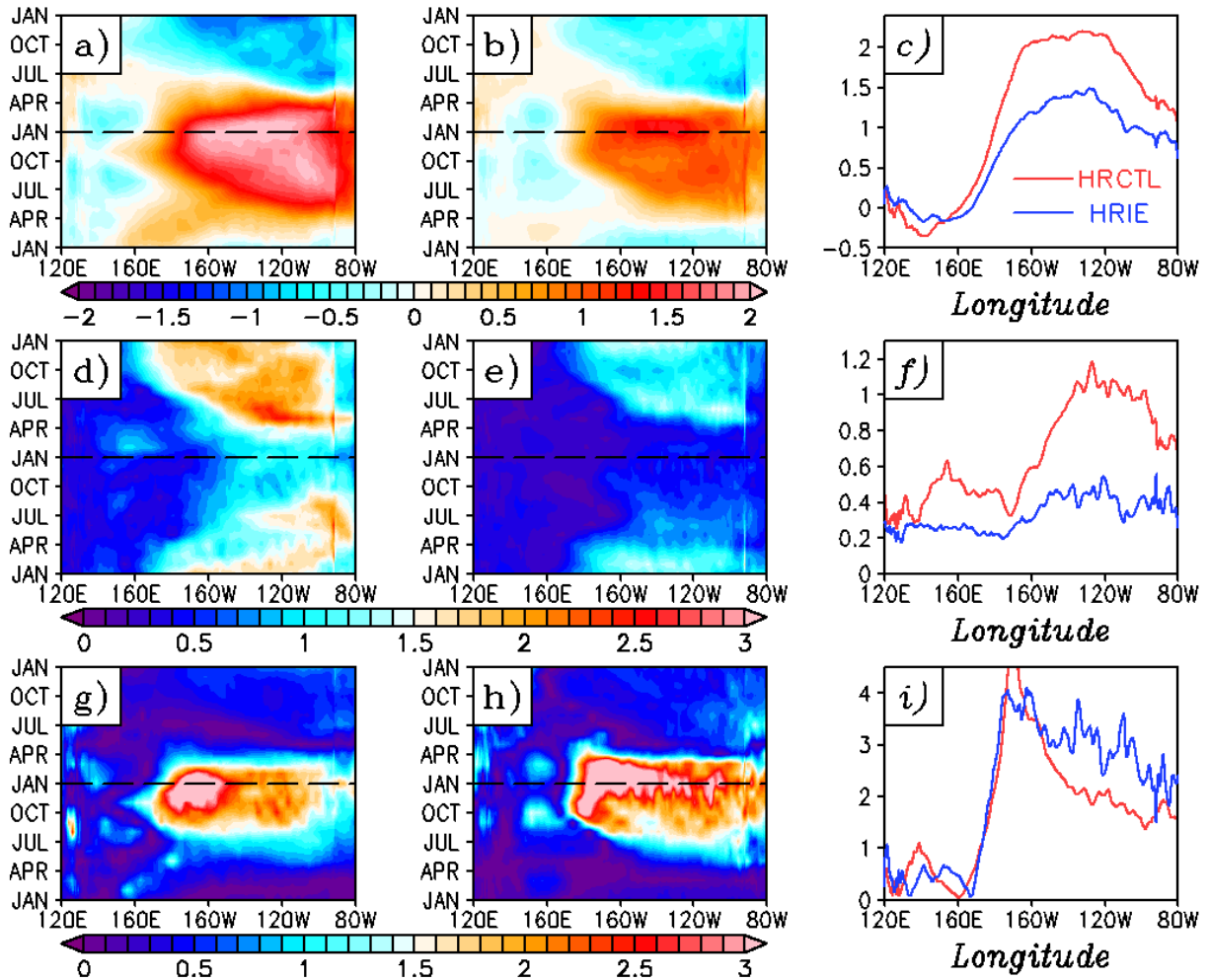
Figure 12. Composite evolution of SSTA (°C) along the equatorial Pacific during the 10 El Niño events for HRCTL a) and HRIE b) and cross-equatorial SSTA structure at zero-lag c). Similarly, standard deviation among events (°C) is shown for HRCTL d), HRIE e), and f). Signal-to-noise ratio is described for HRCTL g), HRIE h), and i) where this is defined by the ratio of the magnitude of composite SSTA over the standard deviation among events. Composite is based on DJF Niño3.4 SSTA and centered (zero-lag) on the dashed horizontal line with time increasing up the page.
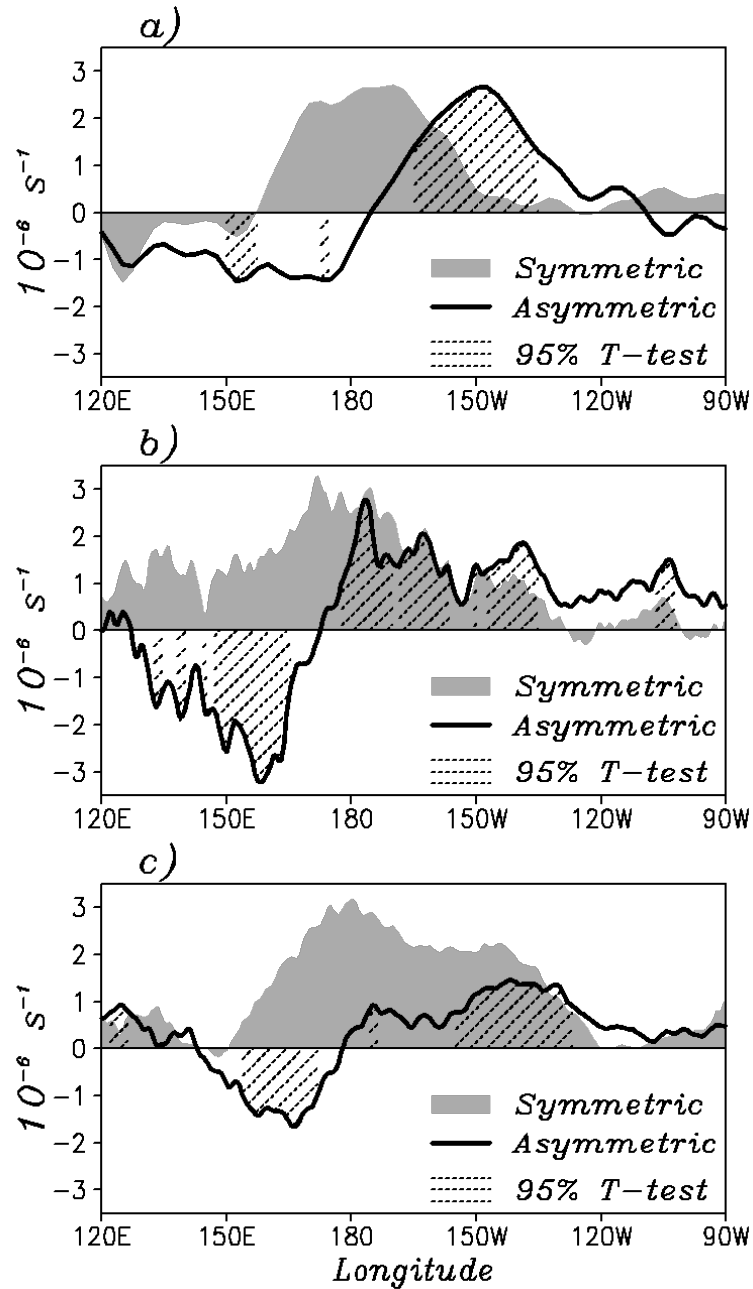
Figure 13. Composite of observed a), HRCTL b), and HRIE c) symmetric (i.e., El Niño minus La Niña divided by 2, shaded grey) and asymmetric (El Niño plus La Niña, black line) components of 200 hPa anomalous divergence meridionally averaged (5°S to 5°N) across the Pacific Ocean. Dotted shade indicates where the asymmetry is distinct from zero at 95% confidence level from a student-T test. The analysis of HRIE model is performed on the ensemble mean from the 10 atmospheres realization.
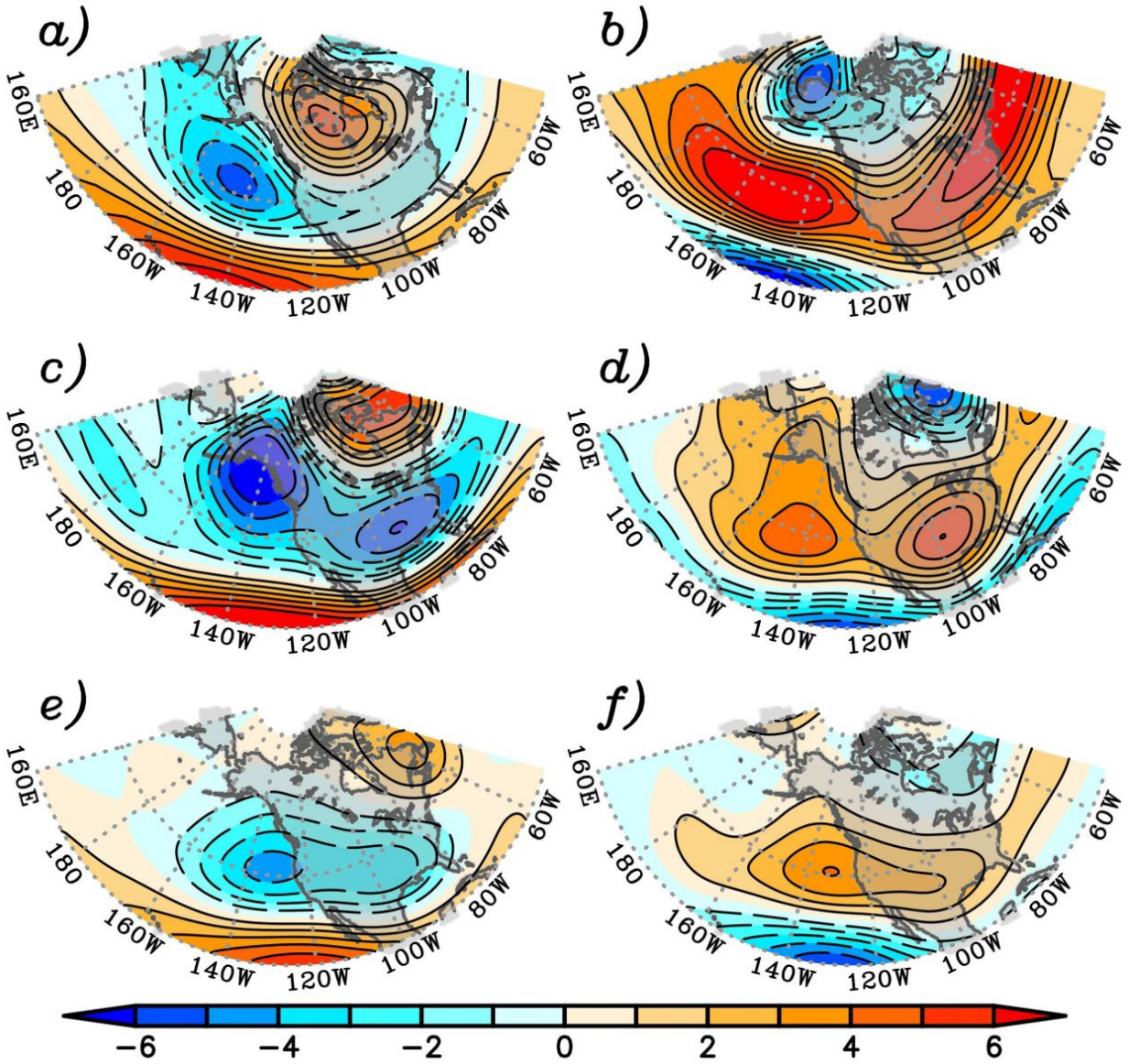
Figure 14. Composite of 200 hPa streamfunction anomaly (10^6 s^{-1}) for boreal winters (DJF) during El Niño events: observed a), HRCTL c), and HRIE e). Similarly, for La Niña events: observed b), HRCTL d), and HRIE f).
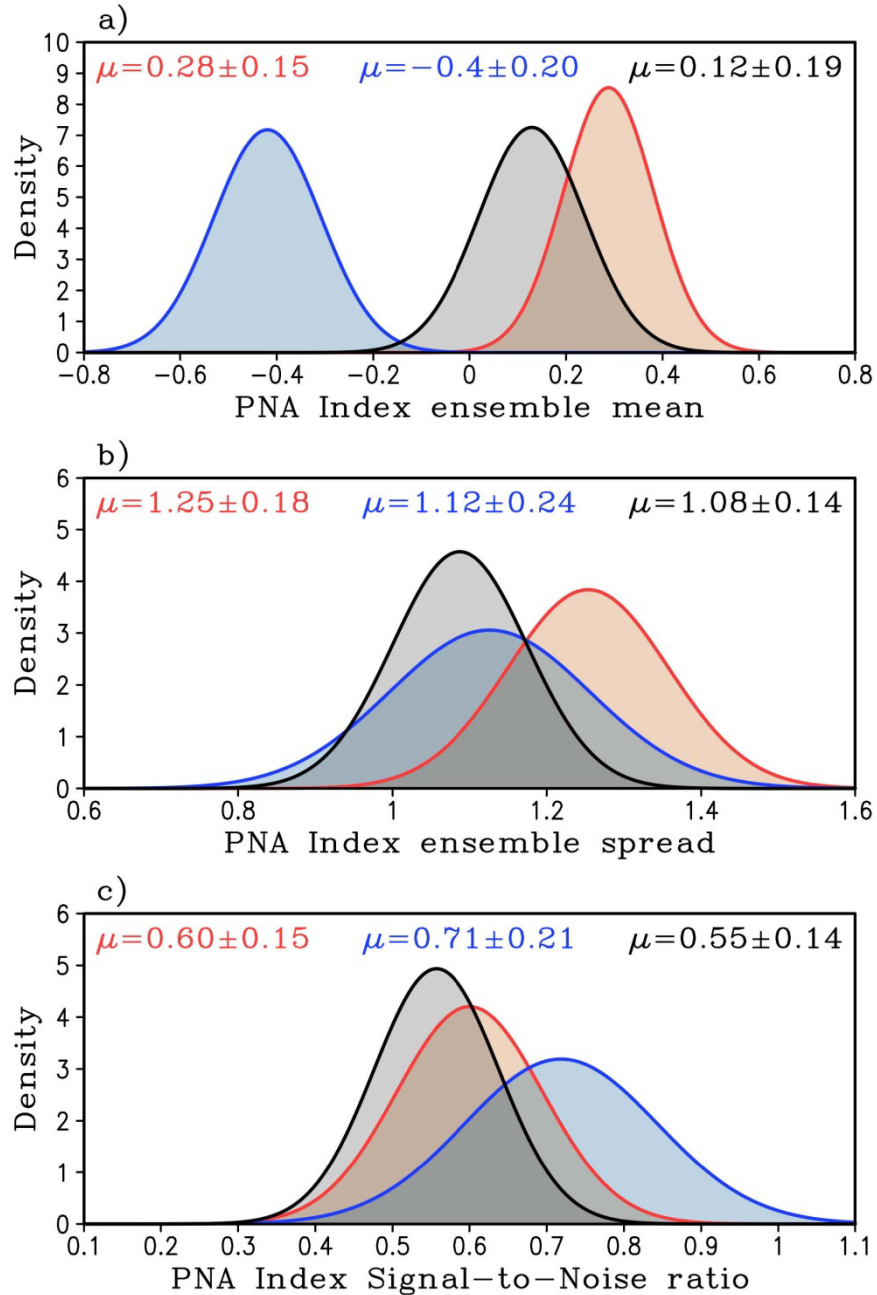
60

Figure 15. Probability density function (PDF) of the PNA index conditioned by the state of Niño3.4 SSTA for El Niño (red), La Niña (blue), and neutral conditions (gray) in the HRIE experiment. a) The ensemble mean PNA index, b) the ensemble spread of the PNA index, and c) the signal-to-noise ratio (SNR). The PDF were constructed by randomly selecting 6 out of 10 ensemble members from the HRIE experiment and computing the ensemble mean, spread, and SNR for each realization, this was repeated 1000 times. The mean plus the 95th percentile is shown at the top of each panel.
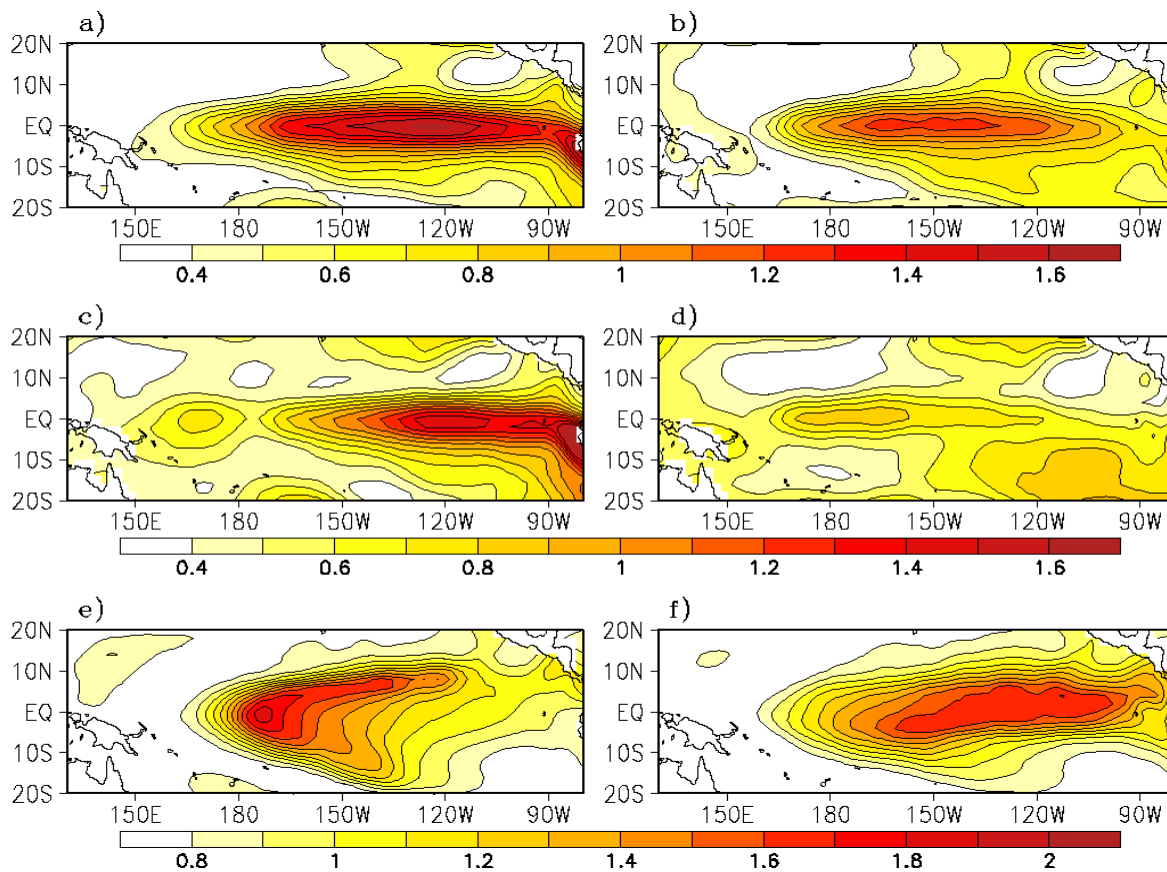
Figure 16. a) Ensemble mean (i.e., signal), c) ensemble spread (i.e., noise), and e) signal-to-noise ratio of observed SST anomaly during El Niño events for the period of 1950-2017. Panels b), d), and f) are similar to a), c), and e) but for La Niña SST anomalies. The ensemble mean is taken as the root mean square of SST anomalies for all events. The ensemble spread is the root mean square difference of SST anomalies among all ENSO events (i.e., inter-event variance or diversity). The calculations were performed for December-January-February SST anomaly.
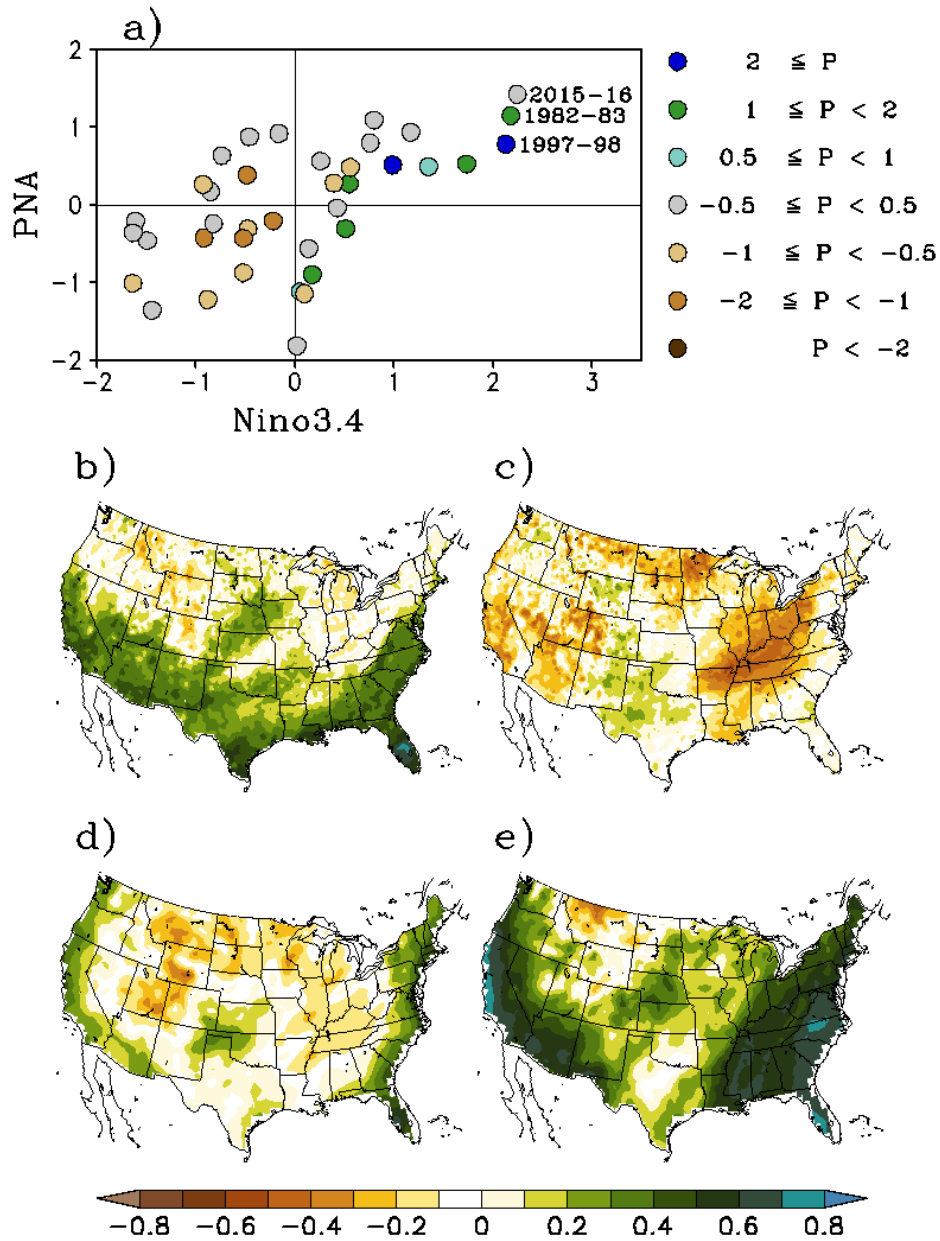
Figure 17. a) Scatter diagram showing the observed Niño3.4 SSTA index versus PNA index. The color-coding is with respect to boreal winter standardize precipitation anomaly over California. The three strongest El Niño events of 1982-83, 1997-98, and 2015-16 are highlighted. Also showing the partial correlation of observed precipitation over North America with b) Niño3.4 SSTA and c) PNA index during boreal winter (DJF). Partial correlation of precipitation anomaly with Niño3.4 for d) HRCTL and e) HRIE experiments. Here, the influence of the PNA index is held constant. Partial correlation separates the effect of each index on the dependent variable with the influence of the remaining or other indices held constant.